Supplementary Information: Rotor-stator repulsion and medium-induced dephasing enhance and equalise the quantum efficiency of a fluorinated photon-only rotary motor

Michael Filatov(Gulak),[*,†] Meseret Simachew Bezabih,[‡] Marco Paolino,[¶] Massimo Olivucci,[*,¶,‡] and Seung Kyu Min[*,§,†]

†*Center for Multidimensional Carbon Materials, Institute for Basic Science (IBS), UNIST-gil 50, Ulsan, 44919, Republic of Korea*

‡*Chemistry Department and Center of Photochemical Sciences, Bowling Green State University, Overmann Hall, Bowling Green, 43403, OH, USA*

¶*Dipartimento di Biotecnologie, Chimica e Farmacia, Università di Siena, Via A. Moro 2, 53100 Siena, Italy*

§*Department of Chemistry, Ulsan National Institute of Science and Technology (UNIST), UNIST-gil 50, Ulsan, 44919, Republic of Korea*

E-mail: mike.filatov@gmail.com; massimo.olivucci@unisi.it; skmin@unist.ac.kr

Contents

1 Supplementary Note 1. List of acronyms used in the main article

CoIn	Conical Intersection
CCW	Counterclockwise
CW	Clockwise
DBPI	double bond photoisomerisation
eDFT	ensemble density functional theory
FC	Franck-Condon
LDRM	Light Driven Rotary Motor
MCP	3-methylene-1-cyclopentene
MMTDP	*E*-1-methyl-3′-(2-methyl-2,3-dihydro-1H-benzo[b]cyclopenta[d]thiophen-1-ylidene)pyrrolidin-2′-one
MTDP	*E*-3′-(2-methyl-2,3-dihydro-1H-benzo[b]cyclopenta[d]thiophen-1-ylidene)pyrrolidin-2′-one
NAMD	nonadiabatic molecular dynamics
OA	overcrowded alkene
PES	potential energy surface
PO-LDRM	Photon Only Light Driven Rotary Motor
QM/MM	quantum mechanics / molecular mechanics (multi-scale modelling technique)
SI	Supporting Information
SSR	State-interaction State-averaged spin-Restricted ensemble-referenced Kohn-Sham method
THI	Thermal Helix Inversion
TSH	trajectory surface-hopping

2 Supplementary Note 2. Synthetic route to fluorine substituted motor

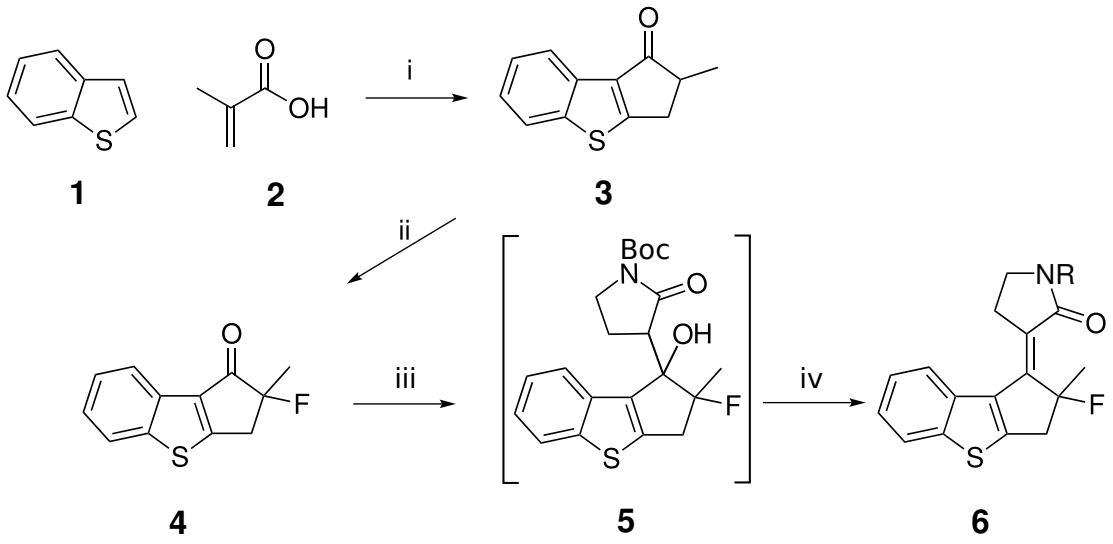

Supplementary Figure 1: Synthetic procedure for obtaining fluorine substituted molecular motor. Reagents: (i) PPA, 80 °C;[1] (ii) LiHMDS, toluene, NFSI, -78 °C;[2] (iii) LiHMDS, N-Boc pyrrolidin-2-one, BF3O(Et)2, THF, -78 °C; (iv) TFA, DCM.

Starting from benzothiophene and metacrylic acid, two commercially available products, as already shown in previous works[1], it is possible to synthesize the 2-methyl-2,3-dihydro-1H-benzo[b]cyclopenta[d]thiophen-1-one nucleus, **3** in Supplementary Fig. 1. The insertion of a fluorine atom in the alpha position to the carbonyl in **3** can be carried out using N-fluorobenzenesulfonimide (NFSI) in the presence of lithium bis(trimethylsilyl)amide (LiHDMS) as a base in a strongly anhydrous environment in order to obtain the racemic mixture of the fluorinated nucleus **4** by applying the synthetic procedure reported in the literature by Štacko et al..[2] Finally, similarly to what was done for the synthesis of the non-fluorinated compound ,[3,4] it is possible to first condense the pyrrolidinone head using LiHDMS as a base to obtain an enantiomeric mixture of carbinol derivatives (**5**) which, following dehydration with trifluoroacetic acid, allow obtaining the R,S racemic mixture of the desired product (**6**)

equipped with the isomerizable double bond.

3 Supplementary Note 3. Computational Methods

SSR method

The SSR method[5–10] employed in this work to obtain the ground and excited electronic states energies, forces on the nuclei (the analytic gradient), and the non-adiabatic coupling (NAC) vector employs ground state eDFT[11–16] to describe the non-dynamic electron correlation occurring due to multireference character of the ground state and eDFT for ensembles of ground and excited states[17–20] to obtain excitation energies from a variational time-independent formalism. The ensemble representation of the density and energy of a strongly correlated electronic state results in occurrence of the fractional occupation numbers (FONs) of several frontier KS orbitals. Here, the SSR(2,2) method is used, where two fractionally occupied orbitals accommodate two electrons in total. The energies of the ground S_0 and excited S_1 states are obtained in SSR(2,2) from variational optimization of an ensemble of a perfectly spin-paired singlet (PPS) electronic configuration and an open-shell singlet (OSS) configuration with respect to the KS orbitals and their FONs (the SA-REKS(2,2)[7] orbital optimization), which is followed by solving a 2×2 secular problem

$$\begin{pmatrix} E_0^{PPS} & \Delta_{01}^{SA} \\ \Delta_{01}^{SA} & E_1^{OSS} \end{pmatrix} \begin{pmatrix} a_{00} & a_{01} \\ a_{10} & a_{11} \end{pmatrix} = \begin{pmatrix} E_{S_0} & 0 \\ 0 & E_{S_1} \end{pmatrix} \begin{pmatrix} a_{00} & a_{01} \\ a_{10} & a_{11} \end{pmatrix} \tag{1}$$

for the actual S_0 and S_1 states.[8–10] The interstate coupling parameter Δ_{01}^{SA} is calculated simultaneously with the E_0^{PPS} and E_1^{OSS} energies when optimizing the KS orbitals (and their FONs) in the SA-REKS(2,2) calculation.[8–10]

For the S_0 and S_1 energies, the analytic gradients are available.[21–23] The gradients of

the S_0 and S_1 states are related to the gradients of the PPS and OSS states and the coupling element Δ_{01}^{SA} as

$$\boldsymbol{\nabla} E_{S_k} = a_{kk}^2 \boldsymbol{\nabla} E_0^{PPS} + a_{lk}^2 \boldsymbol{\nabla} E_1^{OSS} + 2\, a_{kk}\, a_{lk}\, \boldsymbol{\nabla} \Delta_{01}^{SA}\,; \quad l \neq k\,; \quad l,k = 0,1 \tag{2}$$

SHXF method

The SHXF method has been described in detail elsewhere[24,25] and here only a brief account of its basic features will be given. The SHXF method combines the electronic equations derived from the exact factorization of the electronic-nuclear wavefunction[26–30] with the conventional TSH formalism.[31] The exact factorization enables one to seamlessly incorporate the effect of nuclear quantum momentum, which depends on the shape of nuclear distribution, into the classical equations of motion for the nuclei.

SHXF is a mixed quantum-classical method where the electronic degrees of freedom are treated quantum mechanically and the classical description in terms of trajectories is used for the nuclear degrees of freedom. For a given nuclear trajectory $\mathbf{R}^{(I)}$, the time-dependent electronic wavefunction $\Phi_{\mathbf{R}^{(\mathrm{I})}}(\mathbf{r}, t)$ is expanded in terms of the wavefunctions of the Born-Oppenheimer (BO) states as $\Phi_{\mathbf{R}^{(\mathrm{I})}}(\mathbf{r}, t) = \sum_l C_l^{(I)}(t)\phi_l(\mathbf{r}; \mathbf{R}^{(I)}(t))$ and the time evolution of an element $\rho_{lk}^{(I)}(t) = C_l^{(I)*}(t)C_k^{(I)}(t)$ of the reduced density matrix $\rho^{(I)}(t)$ is described by

$$\begin{aligned}\frac{d}{dt}\rho_{lk}^{(I)}(t) =& \frac{i}{\hbar}\left\{E_l^{(I)}(t) - E_k^{(I)}(t)\right\}\rho_{lk}^{(I)}(t) - \sum_j \left\{\sigma_{lj}^{(I)}(t)\rho_{jk}^{(I)}(t) - \rho_{lj}^{(I)}(t)\sigma_{jk}^{(I)}(t)\right\} \\ &+ \sum_j \left\{Q_{jl}^{(I)}(t) + Q_{jk}^{(I)}(t)\right\}\rho_{lj}^{(I)}(t)\rho_{jk}^{(I)}(t)\end{aligned} \tag{3}$$

where $E_l^{(I)}$ and $\phi_l(\mathbf{r}; \mathbf{R}^{(I)}(t))$ are the energy and the wavefunction of the l-th BO state, $\sigma_{jk}^{(I)}$ is a non-adiabatic coupling matrix element between the jth and kth BO electronic

states, and $Q_{jk}^{(I)}$ is a term that gives quantum correction to the nuclear motion arising from electronic-nuclear correlations;[28–30] the latter term is derived from the exact factorization of the electronic-nuclear wavefunction.[24] In Eq. (3),the superscript (I) indicates a quantity obtained at the nuclear configuration $\mathbf{R}^{(I)}$.

In Eq. (3), the $Q_{jk}^{(I)}$ term yields coupling between the nuclear quantum momenta $i\hbar\nabla_\nu|\chi|/|\chi|$ and the electronic phases $\mathbf{f}_{\nu,j}^{(I)}$ and $\mathbf{f}_{\nu,k}^{(I)}$

$$Q_{jk}^{(I)} = \sum_\nu \frac{i\hbar}{M_\nu} \frac{\nabla_\nu|\chi|}{|\chi|}\bigg|_{\mathbf{R}^{(I)}(t)} \cdot \left(\mathbf{f}_{\nu,j}^{(I)} - \mathbf{f}_{\nu,k}^{(I)}\right) \tag{4}$$

where M_ν is a mass of the νth nucleus. The nuclear quantum momenta are obtained from a number of auxiliary nuclear trajectories generated for electronic states other than the running state l. Although the concept of auxiliary trajectories for decoherence-induced surface hopping dynamics is not new,[32] the correction used here is derived from the exact quantum equations and no further renormalisation of the electronic density matrix is needed.

An auxiliary trajectory $\mathbf{R}^{(I)}(t')$ is generated when a nonzero $\rho_{kk}(t')$ is encountered at a time t' and is evolved classically with a uniform velocity obtained from the energy conservation law. The electronic phase term $\mathbf{f}_{\nu,k}^{(I)} = -\int^t \nabla_\nu E_k^{(I)}(t')dt'$ is evaluated by time integration of the momentum changes at the kth BO state. To calculate the quantum momentum, a fictitious Gaussian nuclear density $|\chi_k|^2$ with a uniform variance σ is associated with the auxiliary trajectory at each BO state. Then, the nuclear quantum momentum is $\nabla_\nu|\chi|/|\chi|(\mathbf{R}^{(\mathbf{I})}(\mathbf{t})) = -\frac{1}{2\sigma^2}(R_\nu^{(I)}(t) - \langle R_\nu^{(I)}(t)\rangle)$, where $\langle R_\nu^{(I)}(t)\rangle = \sum_k \rho_{kk}^{(I)} R_{k\nu}^{(I)}(t)$. The uniform variance σ can be either obtained from the initial distribution of nuclear trajectories or set as a parameter. Here, a uniform value $\sigma = 0.1$ a.u. is used.

Nuclear trajectories follow the Newtonian equations of motion on the PES of the running state l, *i.e.*, the force on the νth nucleus is $\mathbf{F}_\nu^{(I)} = -\nabla_\nu E_l^{(I)}$. When the surface

hop probability becomes greater than a random number, a surface hop is initiated. The surface hop probability from the running state l to another state $k(\neq l)$ at a time interval $[t, t+\Delta t]$ is calculated as

$$P_{l\to k} = \frac{2\Re\left[\rho_{lk}^{(I)}(t)\sigma_{lk}^{(I)}(t)\right]}{\rho_{ll}^{(I)}(t)}\Delta t\,, \tag{5}$$

where the same constraints as in the Tully's fewest switches algorithm[31,33] are imposed on the hopping transition; *i.e.*, when $E_k^{(I)}$ is greater than the total energy, the transition is forbidden and, when a negative hopping probability is obtained (*e.g.*, due to the phase factor of $\rho_{lk}^{(I)}(t)$), the probability is set to zero. Upon a successful surface hop, the nuclear velocities are rescaled to satisfy the total energy conservation, and the running state is switched to the new state.

Computational details

All the quantum chemical computations were carried out using the local version of the GAMESS-US program (2018.v3),[34,35] which implements the SSR method and the analytic derivatives formalism.[21] All the calculations employed the 6-31G* basis set[36] and the BH&HLYP exchange-correlation density functional.[37–39] The geometry optimizations were performed using the DL-FIND module[40] interfaced with GAMESS-US.

The QM/MM NAMD simulations were performed by the pyUNIxMD program,[25,41] a standalone code which implements the SHXF method.[24] The energy gradients $\boldsymbol{\nabla} E_{S_k}$ ($k = 0, 1$) were calculated by the GAMESS-US program. The nonadiabatic couplings were obtained using the Baeck-An method,[42–45] which operates with the energies of the ground and excited states alone. The nuclear equations of motion were integrated using the velocity-Verlet algorithm with the time step of 0.5 fs. The electronic equations of motion (3) were integrated by the 4-th order Runge-Kutta method with the time step of 0.025 fs. When integrating the electronic equations of motion, the electronic energies $E_l^{(I)}$

and the nonadiabatic couplings $\sigma_{lk}^{(I)}$ were linearly interpolated between the end points of the integration interval of the nuclear equations of motion.

The QM/MM calculations were performed by the GAMESS-US program interfaced with TINKER program v6.3.[46] The force field calculations of the solvent molecules employed the OPLS-AA force field.[47]

4 Supplementary Note 4. Geometry optimization of the ground and excited state stationary species

As a reference, the reaction path and dynamics of F-MMTDP were first studied under isolated conditions. The geometries of the S_0 and S_1 stationary points have been optimised using the DL-FIND code[40] interfaced with GAMESS-US. The convergence criteria used in the optimization of the S_0 and S_1 stationary geometries were set to $\Delta E = 10^{-6}$ hartree and $\Delta|\partial E/\partial r_k| = 4.5 \cdot 10^{-4}$ hartree/bohr. The geometries of the S_1/S_0 conical intersections were optimized using the penalty function algorithm as implemented in DL-FIND code,[40] where the penalty function constants C_1 and C_2 were set to default values (5 kcal mol^{-1}).[40]

The optimized geometries are shown in the graphics form in Supplementary Figs. 2, 3, and 4. Their relative energies and selected geometric parameters are collected in Supplementary Table 1. According to SSR geometry optimisation (see Supplementary Figs. 2, 3, and 4 and Supplementary Table 1) the most stable S_0 structure is **3**-*Z*P (with θ = 6.1° and τ = 30.4°; its energy is taken as the origin of the energy scale) and **3**-*E*P (θ = 189.2°, τ = 22.3°) is 1.2 kcal/mol less stable. This is different from MTDP and MMTDP, where *E*P was the most stable structure (by $\approx$ 4 kcal mol^{-1}).[4,48,49] The difference in relative stabilities of the *E* and *Z* structures is explained by the effect of electrostatic repulsion between the carbonyl oxygen and fluorine atom at the C_7 chiral centre, which was absent in MTDP and MMTDP.

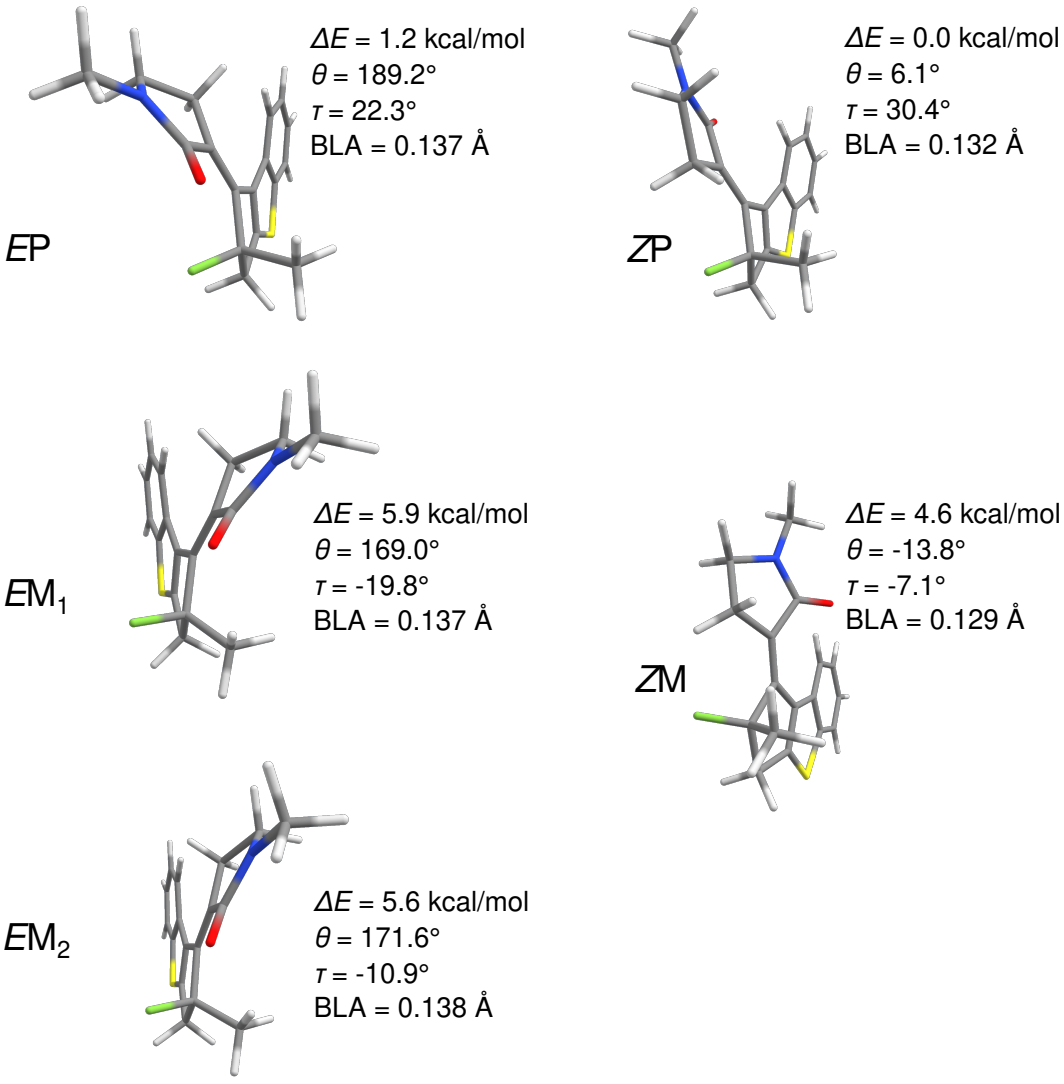

Supplementary Figure 2: Geometries of the local minima on the S_0 potential energy surface of **3** optimised using the SSR-BH&HLYP/6-31G* method. The relative energies (kcal/mol, with respect to the ZP structure) and some important geometric characteristics are given in the insets. See Supplementary Figure 6 for positions of the optimised structures on the global potential energy surface of the motor **3**.

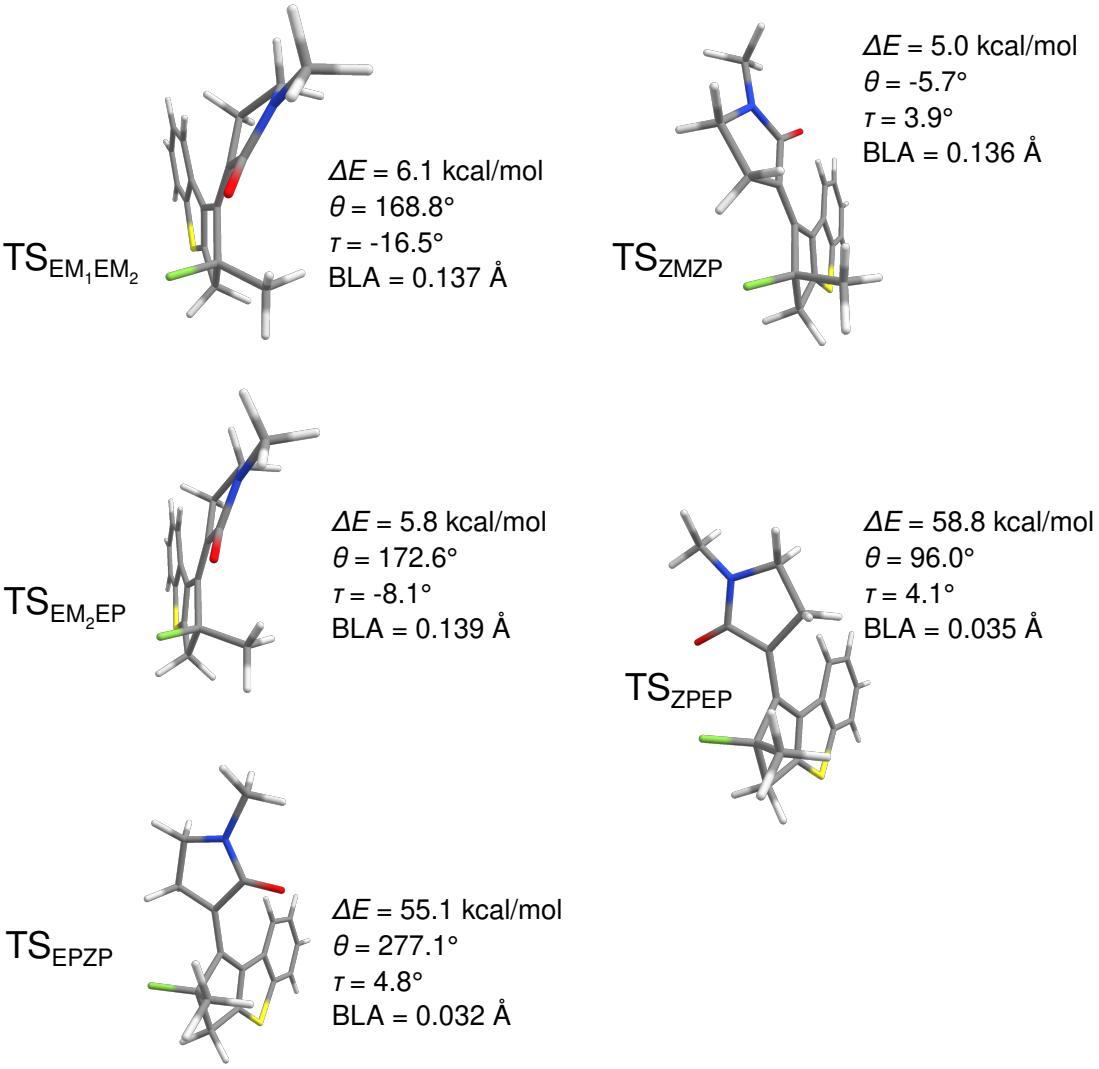

Supplementary Figure 3: Geometries of the transition states on the S_0 potential energy surface of **3** optimised using the SSR-BH&HLYP/6-31G* method. The relative energies (kcal/mol, with respect to the ZP structure) and some important geometric characteristics are given in the insets. See Supplementary Figure 6 for positions of the optimised structures on the global potential energy surface of the motor **3**.

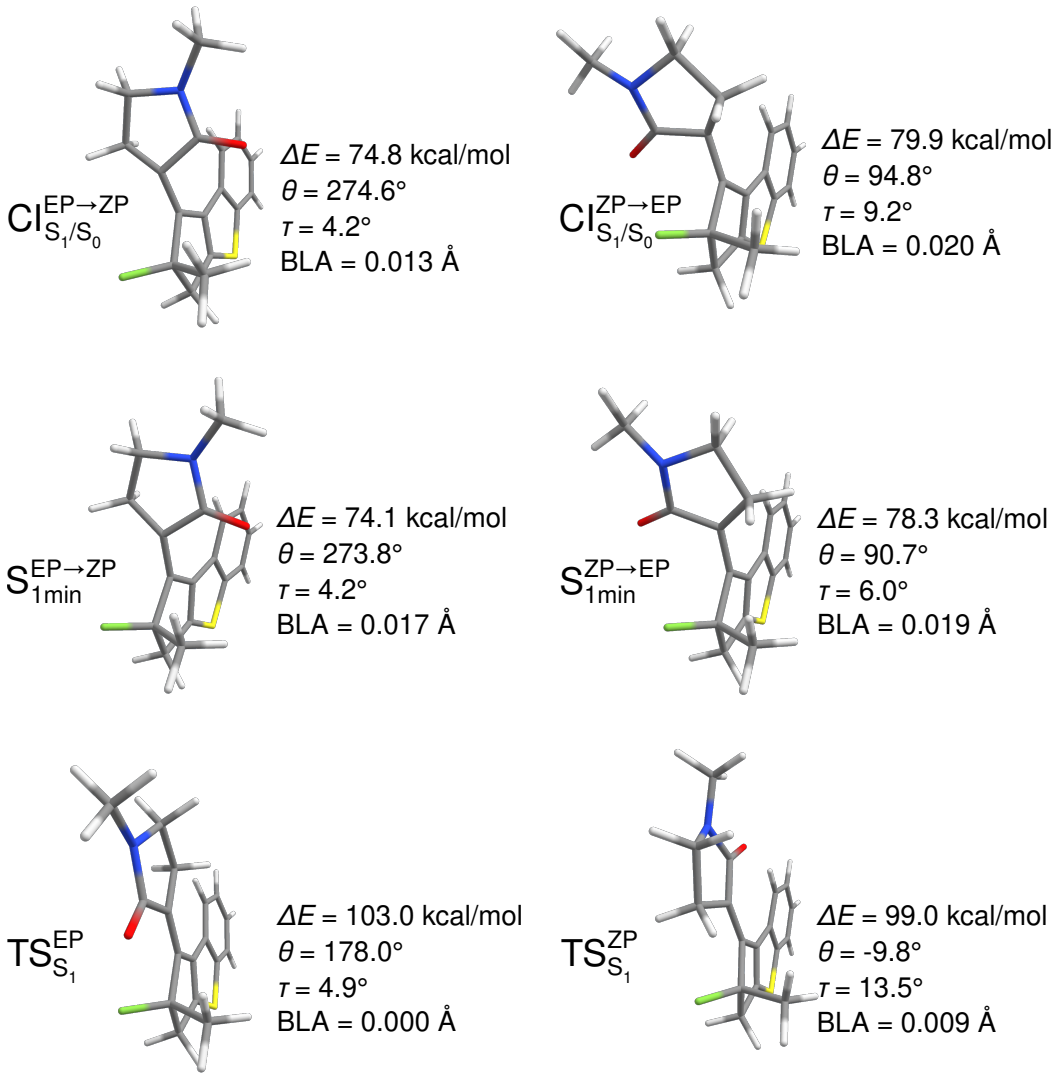

Supplementary Figure 4: Geometries of the minimum energy S_1/S_0 conical intersections, local minima and transition states on the S_1 potential energy surface of **3** optimised using the SSR-BH&HLYP/6-31G* method. The relative energies (kcal/mol, with respect to the ZP structure) and some important geometric characteristics are given in the insets. See Supplementary Figure 6 for positions of the optimised structures on the global potential energy surface of the motor **3**.

Supplementary Table 1: Relative energies (in kcal/mol) and selected geometric parameters of the stationary points on the S_0 and S_1 potential energy surfaces of the motor 3 optimised using the SSR-BH&HLYP/6-31G* method. The central dihedral angle θ, tilting angle τ and Cremer-Pople puckering angle are given in degrees (deg.). The bond length alternation and puckering amplitude are given in Å. See Supplementary Figures 2, 3, and 4 for graphical representation of the structures.

						pyrrolidinone[b]		cyclopentene	
structure	$\Delta E(S_0)$[a]	$\Delta E(S_1)$	θ	τ	BLA	q	ϕ	q	ϕ
$EP(S_{0,min})$	**1.2**	110.0	189.2	22.3	0.1368	0.275	351.7	0.209	358.7
$EM_1(S_{0,min})$	**5.9**	112.4	169.0	-19.8	0.1373	0.287	354.0	0.179	355.6
$EM_2(S_{0,min})$	**5.6**	112.1	171.6	-10.9	0.1380	0.244	349.7	0.070	348.6
$ZP(S_{0,min})$	**0.0**	106.4	6.1	30.4	0.1319	0.217	349.0	0.297	359.0
$ZM(S_{0,min})$	**4.6**	107.5	-13.8	-7.1	0.1292	0.286	353.9	0.076	205.0
$TS_{EPZP}(S_0)$	**55.1**	80.3	277.1	4.8	0.0323	0.021	36.6	0.037	4.4
$TS_{ZPEP}(S_0)$	**58.8**	83.8	96.0	4.1	0.0351	0.125	330.0	0.114	14.5
$TS_{EM_1EM_2}(S_0)$	**6.0**	112.1	168.8	-16.5	0.1369	0.279	352.2	0.140	356.1
$TS_{EM_2EP}(S_0)$	**5.8**	112.4	172.6	-8.1	0.1385	0.217	345.6	0.025	280.8
$TS_{ZMZP}(S_0)$	**5.0**	110.8	-5.7	3.9	0.1361	0.303	2.6	0.122	3.3
$CI_{S_1/S_0}^{EP\rightarrow ZP}$	74.8	**74.8**	274.6	4.2	0.0128	0.347	342.5	0.125	4.2
$CI_{S_1/S_0}^{ZP\rightarrow EP}$	79.9	**79.9**	94.8	9.2	0.0203	0.374	349.1	0.220	356.8
$S_{1,min}^{EP\rightarrow ZP}$	65.9	**74.1**	273.8	4.2	0.0166	0.322	336.9	0.117	7.2
$S_{1,min}^{ZP\rightarrow EP}$	66.8	**78.3**	90.7	6.0	0.0192	0.313	338.5	0.133	4.3
$TS_{S_1}^{EP}$	15.5	**103.0**	178.0	4.9	0.0002	0.141	313.1	0.123	28.4
$TS_{S_1}^{ZP}$	12.7	**99.0**	-9.8	13.5	0.0096	0.230	331.3	0.224	7.3

[a] All energies are given with respect to the most stable ground state structure, ZP. The energy of the optimised structure is highlighted. The other energy is obtained by a vertical excitation/deexcitation.
[b] Cremer-Pople ring puckering parameters[50] of the respective 5-membered rings, the puckering amplitude q and puckering angle ϕ. The puckering coordinates are pivoted at the $C_{4'}$ atom for the pyrrolidinone ring and C_7 atom for the cyclopentene ring. See also atomic numbering in Supplementary Figures 19 and 20.

In MTDP and MMTDP, no stable M-helical structures could be obtained in the S_0 state, and the respective regions on the S_0 PES could be best characterised as inflexion points.[4,48,49] However, in F-MMTDP the ground state species with M helicity occur as shoulders on the S_0 PES at $\approx$ 5 kcal/mol above the respective P-minima, and they correspond to very shallow local minima separated from the P-minima by barriers of

less than 0.4 kcal/mol; see Supplementary Table 1. With such low barriers, these minima become kinetically unstable because the energy of photoexcitation is on the order of 100 kcal/mol and, during the photodynamics of the motor, this energy is released to the internal vibrational degrees of freedom; thus, heating the motor molecule and enabling easy passage through the shoulders on the S_0 PES. Therefore, F-MMTDP shares, with MTDP and MMTDP, the ability to isomerise without stumbling upon the M-helical structures.

5 Supplementary Note 5. Minimum energy paths

Using the geometries of the stationary species on the S_0 and S_1 potential energy surfaces (PESs), optimisation of minimum energy paths connecting the stationary points has been carried out using the nudged elastic band (NEB) method[51] as implemented in the DL-FIND program.[40] When optimizing the MEPs, the stationary species were first arranged in the order of increasing central dihedral angle θ (for definition of θ, see Fig. 3c in the main article). Then the MEPs between the stationary points were optimised separately on the S_0 and S_1 PESs using 30 to 50 intermediate images between the stationary geometries.

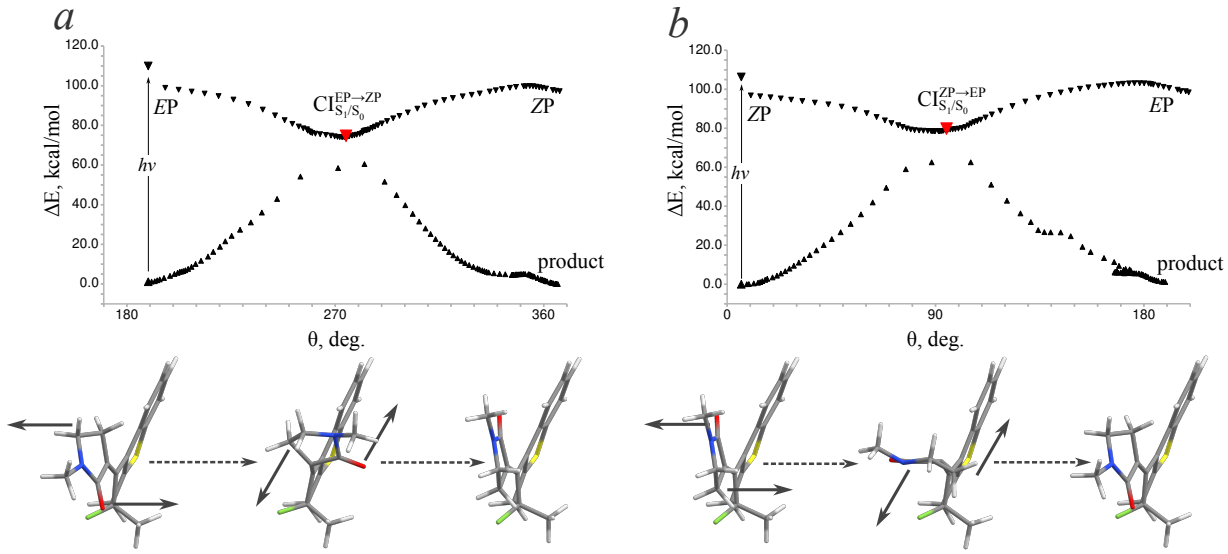

Supplementary Figure 5: Projection of the adiabatic minimum energy paths (MEPs) of the F-MMTDP motor in gas phase onto θ (see Fig. 3c in the main article for the definition of θ) calculated with the SSR-BH&HLYP/6-31G* method. The MEPs optimised for the S_1 state are shown by downward pointing triangles and for the S_0 state by the upward pointing triangles. The structures below the plot show the geometries of the reactants (EP or ZP), the conical intersections (CIs), and the product (ZP or EP). The arrows indicate a CCW motion. Panel (a) shows the EP $\rightarrow$ ZP photoreaction and panel (b) the ZP $\rightarrow$ EP photoreaction. See Supplementary Fig. 6 for a more detailed representation of the MEPs.

Supplementary Fig. 5 shows the potential energy profiles of the S_1 and S_0 states along the minimum energy paths (MEPs) describing the *EP* $\rightarrow$ *ZP* (Supplementary Fig. 5a) and *ZP* $\rightarrow$ *EP* (Supplementary Fig. 5b) photochemical steps. The MEPs are computed

using the nudged elastic band (NEB) method[51] starting in the respective ground state equilibrium structures and propagating towards the S_1/S_0 CIs shown in Supplementary Fig. 5 by downward-pointing red triangles. The MEPs in Supplementary Fig. 5 are shown as functions of the central dihedral angle θ alone. A complete view of the MEPs is shown in Supplementary Figs. 6 and 7, where it is seen that, along the MEPs, a substantial variation of the tilting angle τ occurs in the range between -20° and $+30^\circ$. However, in the regions on the ground-state PES where M-helical structures occur, the energy profile is essentially flat (see the insets in the Supplementary Fig. 6) and no tall barriers obstruct the passage to the P-helical minima. This is also seen in Supplementary Fig. 5, where the shoulders corresponding to M-helical species occur on the S_0 PES near the P-helical minima.

In equilibrium ground state geometries, *E*P and *Z*P, photoexcitation to the S_1 state is achieved by a $\pi \rightarrow \pi^*$ one-electron transition, which is centred around the C_6=$C_{3'}$ axle and has the vertical excitation energy of 4.72 eV for *E*P and 4.61 eV for *Z*P; see Supplementary Table 1. In both structures, *E*P and *Z*P, photoexcitation corresponds to a local transition as confirmed by a small variation in the charge separation between the pyrrolidinone and benzocyclopentathiophene units upon the $S_0 \rightarrow S_1$ excitation; *E*P: from $0.05\bar{e}$ (S_0) to $0.13\bar{e}$ (S_1), and *Z*P: from $0.05\bar{e}$ (S_0) to $0.17\bar{e}$ (S_1).

As a result of the $\pi \rightarrow \pi^*$ transition, the C_6=$C_{3'}$ π-bond is broken and this allows rotation about the axle. However, the first geometric change that occurs along the MEPs is the change in the bond length alternation (BLA) along the $C_{3'}$=C_6–C_{5b}=C_{8a} chain (BLA = $R_{C_6–C_{5b}} - 1/2[R_{C_{3'}=C_6} + R_{C_{5b}=C_{8a}}]$). In the S_0 equilibrium geometry, BLA in the *E*P and *Z*P structures have values of 0.137 Å and 0.132 Å, respectively, which means that the double bonds along the chain are (on average) shorter than the single bond. However, at the next point along the MEP on the S_1 PES, which differs only slightly in the dihedral angle θ from the Franck-Condon (FC) geometry (by $\approx$ 4–6°), the BLA value drops to a near zero value for both structures, *E*P and *Z*P. This geometric change is not reflected in the graphs

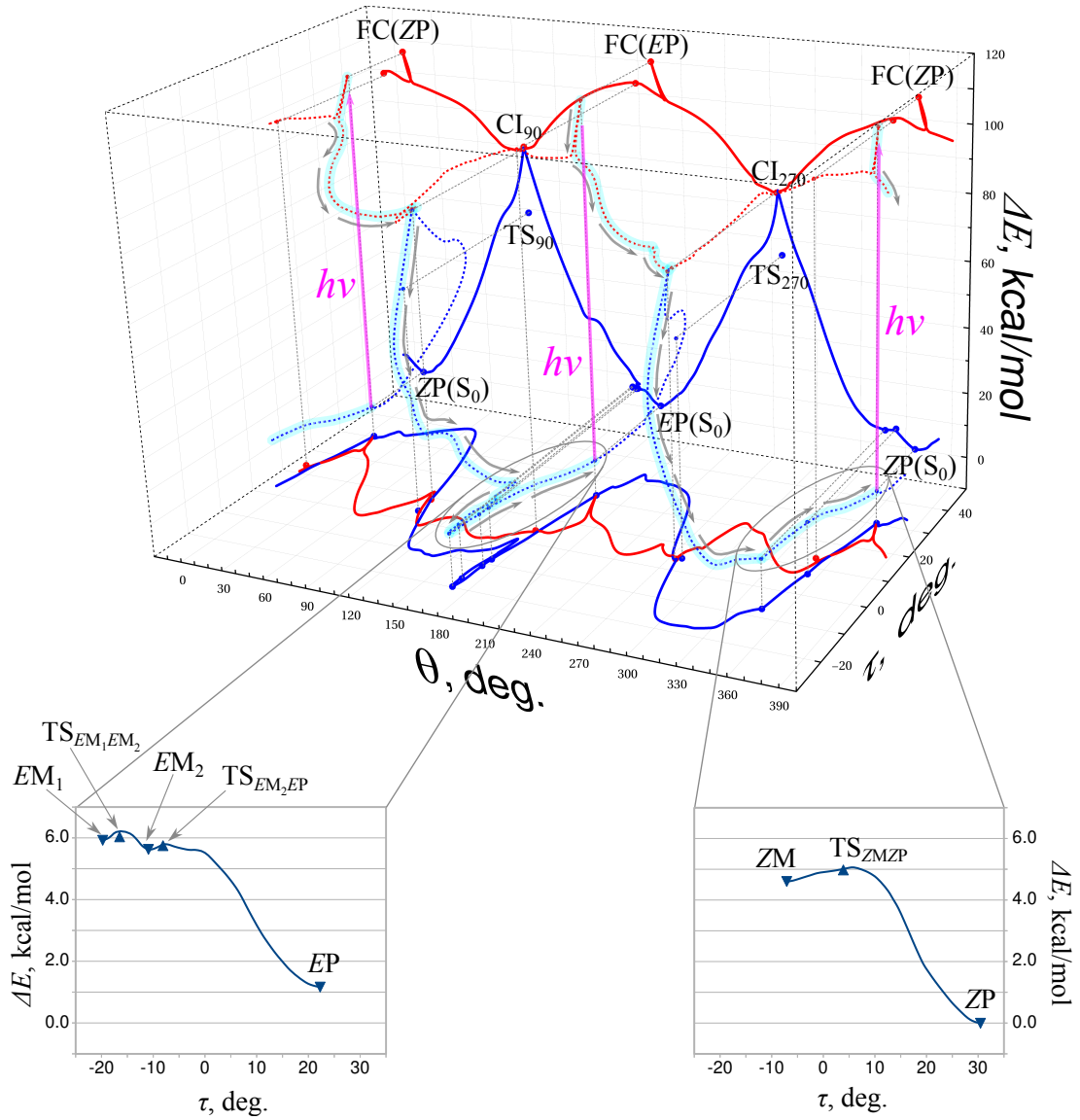

Supplementary Figure 6: Minimum energy paths (MEPs) optimised using the nudged elastic band (NEB) method[51] for the F-MMTDP motor in the gas phase. The MEPs connect the stationary points, minima, transition states (TSs), and conical intersections (CIs), optimised using the SSR-BH&HLYP/6-31G* method. The MEPs are shown as functions of the central dihedral angle θ and tilting angle τ. The red curves show the MEPs optimised for the S_1 state and the blue curves for the S_0 state. The dashed curves show the 3D representation of the MEPs, and the solid curves show projections of the 3D MEPs onto the respective planes. The photoisomerisation path followed by the motor is highlighted on the 3D MEPs by the cyan colour and grey arrows. The insets zoom in on the flat areas on the MEPs designated by grey ellipses.

in Supplementary Fig. 5, however, it should be kept in mind that the elevation of the S_1 FC energy (the black downward-pointing triangles in Supplementary Fig. 5) above the

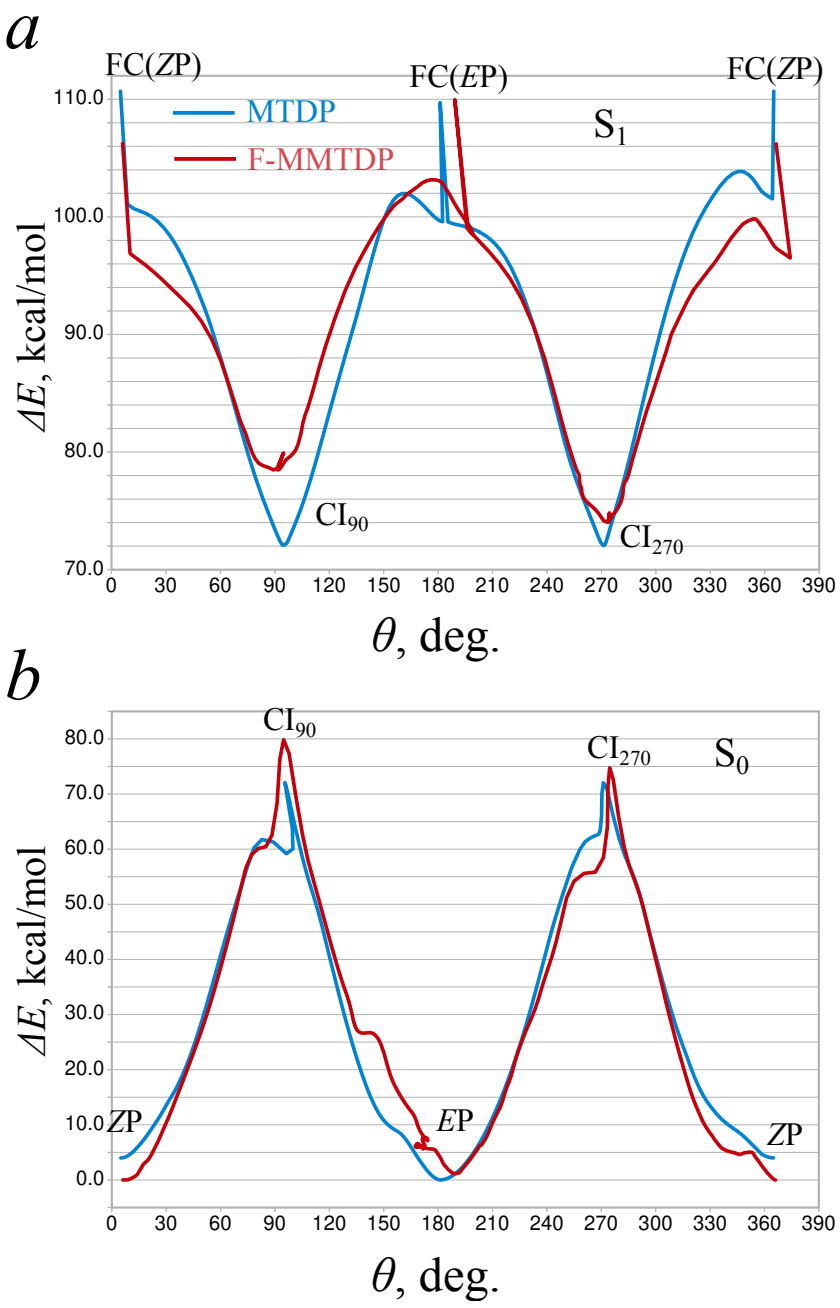

Supplementary Figure 7: Comparison between the MEPs optimised for the S_1 (panel a) and S_0 (panel b) states of the F-MMTDP motor (the red curves) and the original unsubstituted MTDP motor (the blue curves) in the gas phase. The MEPs are given as functions of the central dihedral angle θ.

MEP curves is caused by the change in BLA, without much impacting the torsion angle θ.

Upon undergoing the initial drop in the BLA value, the motor **3** occurs on a slope on the S_1 PES inclined towards increasing angle θ. This facilitates torsion in the CCW

direction towards the S_1/S_0 CIs shown in Supplementary Fig. 5 by the red triangles pointing downward. The driving force for the torsion can be evaluated from the slope of the S_1 PES in the vicinity of the FC geometry and amounts to -0.134 kcal mol^{-1} deg^{-1} ($2.02 \cdot 10^{-4}$ eV rad^{-1}) for the *Z*P structure and to -0.197 kcal mol^{-1} deg^{-1} ($2.97 \cdot 10^{-4}$ eV rad^{-1}) for the *E*P structure. Compared to the parent MTDP motor **1**, the driving force at the FC point increases (in absolute value) almost fourfold for the *E*P structure (from -0.044 kcal mol^{-1} deg^{-1} to -0.197 kcal mol^{-1} deg^{-1}), which results solely from the $C_{2'}$=O$\cdots$F–C_7 intramolecular repulsion. There is also an approximately 36% increase in the driving force at the *Z*P FC geometry, from -0.098 kcal mol^{-1} deg^{-1} in MTDP to -0.134 kcal mol^{-1} deg^{-1} in F-MMTDP. Therefore, the motor **3** should possess a stronger propensity to torsion in the desired direction (CCW) than its predecessors, motors **1** and **2**.

Sliding down the slope on the S_1 PES the motor **3** reaches the S_1/S_0 CIs, which are located near the torsion angle $\theta \approx 270^\circ$ (for *E*P $\rightarrow$ *Z*P) and $\approx 90^\circ$ (for *Z*P $\rightarrow$ *E*P); see Supplementary Fig. 5. Both CIs occur near local minima on the S_1 PES, $S_{1,min}^{EP\rightarrow ZP}$ and $S_{1,min}^{ZP\rightarrow EP}$ in the Supplementary Table 1, and are elevated 0.7–1.6 kcal mol^{-1} above the bottom of the minima. The S_1 state near both the minima and the CIs has charge transfer (CT) characteristics, which are evidenced by the charge separation of $\pm$ 0.55–0.56$\bar{e}$ between the stator (positively charged) and the rotator (negatively charged) units.

The S_1 minima and the CI have the pyrrolidinone ring noticeably puckered, where the Cremer-Pople puckering amplitude[50] q reaches values of $\approx$ 0.32–0.37 Å; see Supplementary Table 1. The pyrrolidinone ring in these geometries attains an envelope conformation (between $^1T_5$ and ^1E) with the puckering angle $\approx$ 340–350°. The S_0 state near these structures shows diradical (DIR) characteristics with a very low charge separation of only $\approx 0.1\bar{e}$. Torsional transition state structures occur on the S_0 PES near the torsion angle θ 277° and 96° at energies almost 20 kcal mol^{-1} below the S_1 local minima and respective CIs. These TSs have almost flat pyrrolidinone rings with

$q \lesssim 0.1$ Å; see Supplementary Table 1. Therefore, the puckering distortion destabilises the ground electronic state, which results in crossing with the S_1 state and the occurrence of CIs. Consequently, the S_1/S_0 CIs occurring in **3**, and **1** and **2**, can be described as the torsion–puckering CIs, as opposed to torsion–pyramidalisation and torsion–BLA CIs observed previously in other LDRM designs.[4,52–55] It is noteworthy that pyrrolidinone pseudo-rotation caused by puckering occurs during the excited state dynamics in all three motors, **1**–**3**, and may affect the outcome of the photoisomerisation.[49] However, a detailed study of this phenomenon goes beyond the scope of the present work and is deferred to a future study.

Having crossed the S_1/S_0 CIs and relaxed to the S_0 state, the motor **3** slides down the S_0 PES towards the isomerised structures; see Supplementary Fig. 5. Typically, branching of the reaction paths occurs at the CI structures, where a fraction of the trajectories in the ensemble continue towards the reaction products and another turns back towards the reactant structures. An accurate fraction of the productive (i.e., propagating towards the products) trajectories in the ensemble can only be determined in molecular dynamics simulations because the photoisomerisation occurs on an ultrafast timescale ($\approx$ 1 ps), which requires the application of NAMD formalism.

Let us summarise the main findings in this section: Substitution in **3** results in a steeper slope of the S_1 PES near the FC geometries and a greater driving force in the desired direction of torsion (CCW). This is expected to eliminate a partial loss of the unidirectionality of rotation, which was observed in the previous two-stroke photon-only LDRMs **1** and **2**.[4,48,49] At the same time, **3** should retain the ability to perform a full 360° loop by consuming light only because there are no sufficiently stable intermediate structures with the opposite helicity, overcoming which would require thermally activated ground state helix inversion steps.

6 Supplementary Note 6. Details of QM/MM simulations

The QM/MM NAMD simulations of F-MMTDP photodecay in three solvents (MeOH, MeCN, and DCM) have been prepared using the protocol described in Ref. 4: After the initial preparation of the target solute molecules, which employed the MP2/6-31G* calculations in connection with the suitably modified OPLS-AA force field,[47] a 5000 ps long molecular dynamics (MD) simulation has been performed under the isothermal-isobaric ensemble (NPT) with the pressure set at 1 atm and temperature at 298 K using the GROMACS software package.[56] During the first 1 ns, the system was gradually thermalised to 298K and equilibrated and, in the subsequent 4 ns, 400 snapshots were selected with 10 ps interval. Each snapshot comprised an approximately 20 Å solvent sphere, which accommodated 906 solvent molecules in the case of MeOH, 668 molecules in MeCN, and 1044 molecules in DCM, see Supplementary Figs. 8, 9, and 10.

The snapshots were used in the construction of the QM/MM models, which employed frozen boundary conditions.[57,58] In the frozen boundary, the solvent molecules have been kept fixed and only the solvent molecules within a sphere of approximately 4 Å radius around the solute molecule have been thawed. For each snapshot, the geometries of the solute molecule and the inner solvent shell have been relaxed in a series of 5 ps QM/MM MD simulations performed in the ground electronic state of the solute molecule at 300K. The MD simulations employed the R-BH&HLYP/6-31G* method in connection with the modified OPLS-AA force field for the solvent molecules. The final snapshots from these MD trajectories were used to initiate the NAMD simulations of F-MMTDP.

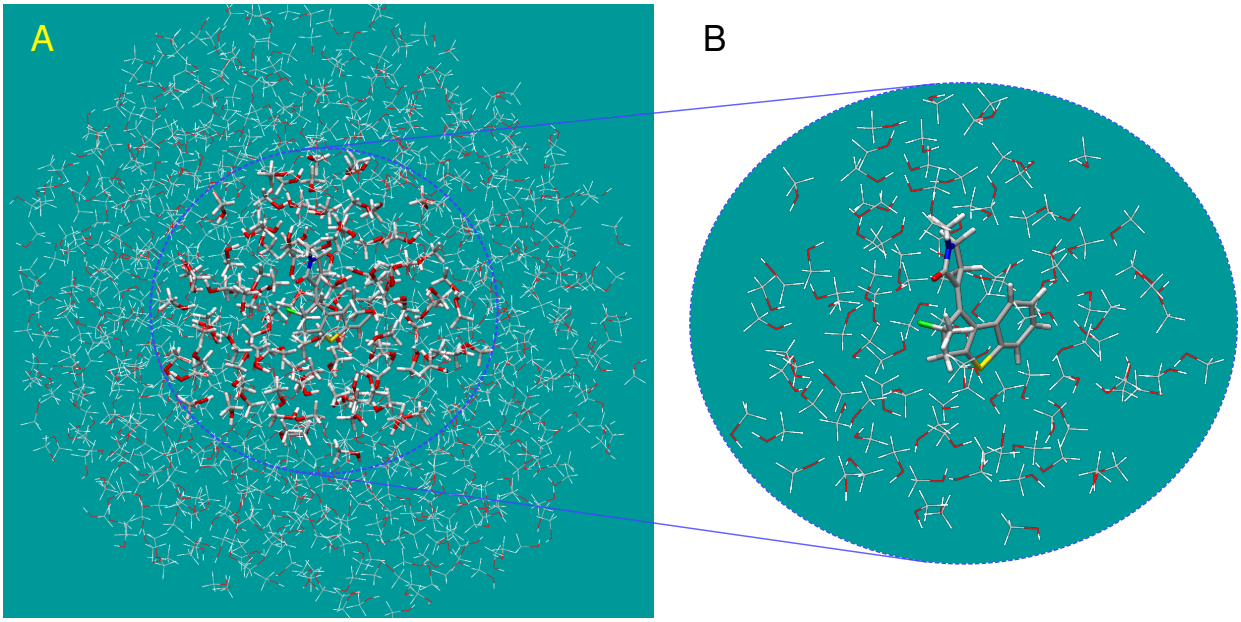

Supplementary Figure 8: The solvent box used in the NAMD QM/MM simulations of the motor **3** in MeOH solution. Panel (A) shows a full box of 906 MeOH molecules and **3**. The circle in the panel (A) highlights the solvation shell of the motor **3**, where the solvent molecules (100 MeOH molecules modelled by MM) and solute molecule (modelled by QM) have been moved during the simulations. The remaining solvent molecules were frozen during the simulations; i.e., the frozen boundary conditions were used. The inset in panel (B) zooms in into the active solvation shell highlighted in panel (A).

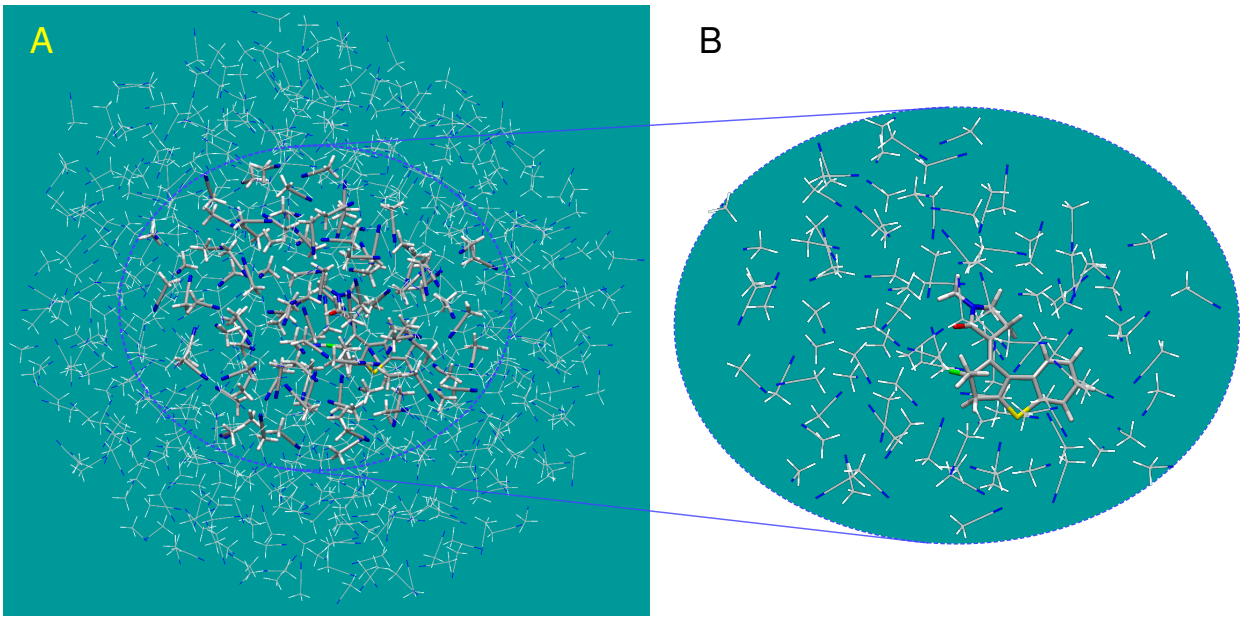

Supplementary Figure 9: The solvent box used in the NAMD QM/MM simulations of the motor **3** in MeCN solution. Panel (A) shows a full box of 668 MeCN molecules and **3**. The circle in the panel (A) highlights the solvation shell of the motor **3**, where the solvent molecules (100 MeCN molecules modelled by MM) and solute molecule (modelled by QM) have been moved during the simulations. The remaining solvent molecules were frozen during the simulations; i.e., the frozen boundary conditions were used. The inset in panel (B) zooms in into the active solvation shell highlighted in panel (A).

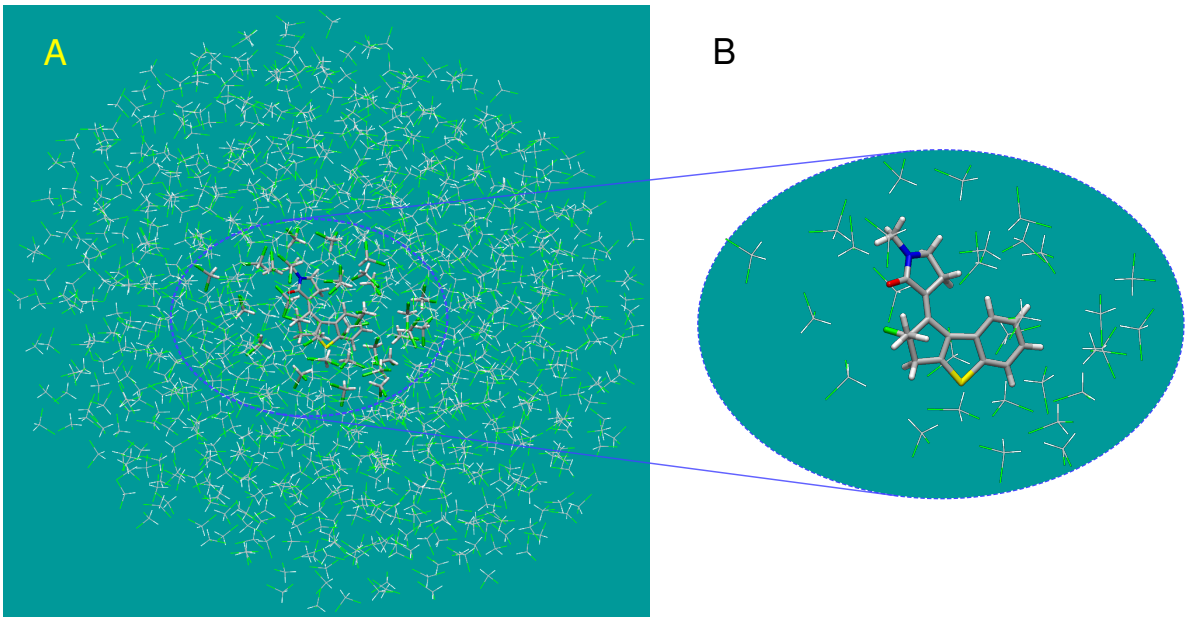

Supplementary Figure 10: The solvent box used in the NAMD QM/MM simulations of the motor **3** in DCM solution. Panel (A) shows a full box of 1044 DCM molecules and **3**. The circle in the panel (A) highlights the solvation shell of the motor **3**, where the solvent molecules (30 DCM molecules modelled by MM) and solute molecule (modelled by QM) have been moved during the simulations. The remaining solvent molecules were frozen during the simulations; i.e., the frozen boundary conditions were used. The inset in panel (B) zooms in into the active solvation shell highlighted in panel (A).

7 Supplementary Note 7. Details of NAMD simulations

The NAMD simulations, both gas phase and QM/MM, employed the SSR(2,2)-BH&HLYP/6-31G* method for obtaining the electronic structure of the solute molecules in the ground and excited states. The initial geometries and nuclear velocities were taken from the previous ground-state MD simulations. Because the SSR/REKS and traditional KS DFT methods yield very close results for the ground states of molecules,[9,10] the use of the initial conditions obtained with KS DFT in lieu of SSR/REKS is justified. The NAMD simulations were carried out using the SHXF method[24,25] implemented in the pyUNIxMD program.[25,41]

In the gas phase NAMD simulations, 50 NAMD trajectories were initiated in the S_1 state in each ground state stationary structure, *E*Pand *Z*P. The trajectories were propagated until the final structure in the S_0 state has been reached. The final S_0 structure was deemed stable, if the dihedral angles θ and τ remained in the range of values characteristic for the *E*Pand *Z*Pstructures (*i.e.*, $\theta \approx 180^\circ$ and $\tau > 0^\circ$ for *E*P, and $\theta \approx 0^\circ$ and $\tau > 0^\circ$ for *Z*P) for approximately 500 fs or longer. Then, the trajectory was terminated. The gas phase simulations have been performed under the microcanonical ensemble (NVE) conditions.

In QM/MM NAMD simulations, 30 trajectories have been initiated in the S_1 state in each ground state stationary structure, *E*Pand *Z*P, and propagated using the SSR(2,2)-BH&HLYP/6-31G* method for a maximum duration of 1500 fs or until the $S_1 \rightarrow S_0$ transition occurred. After the $S_1 \rightarrow S_0$ surface hop, the trajectory has been allowed to continue on the S_0 PES until a S_1–S_0 energy gap became $\gtrsim$ 3 eV. Then, the trajectory has been continued on the S_0 PES using the conventional RKS-BH&HLYP/6-31G* method. Because the SSR and the traditional RKS methods yield very close energies for the ground states of the closed-shell single-reference molecules, this procedure is justified. Typically, the energy difference between the SSR and RKS methods for the same ground state geometry along a trajectory is $\lesssim$ 1.5 kcal mol^{-1}. The RKS-BH&HLYP/6-31G*

QM/MM NAMD simulations have been continued until a stable final structure has been reached. The NAMD and the ground-state MD simulations were performed under the microcanonical ensemble (NVE) conditions.

8 Supplementary Note 8. The results of the gas phase and QM/MM NAMD simulations

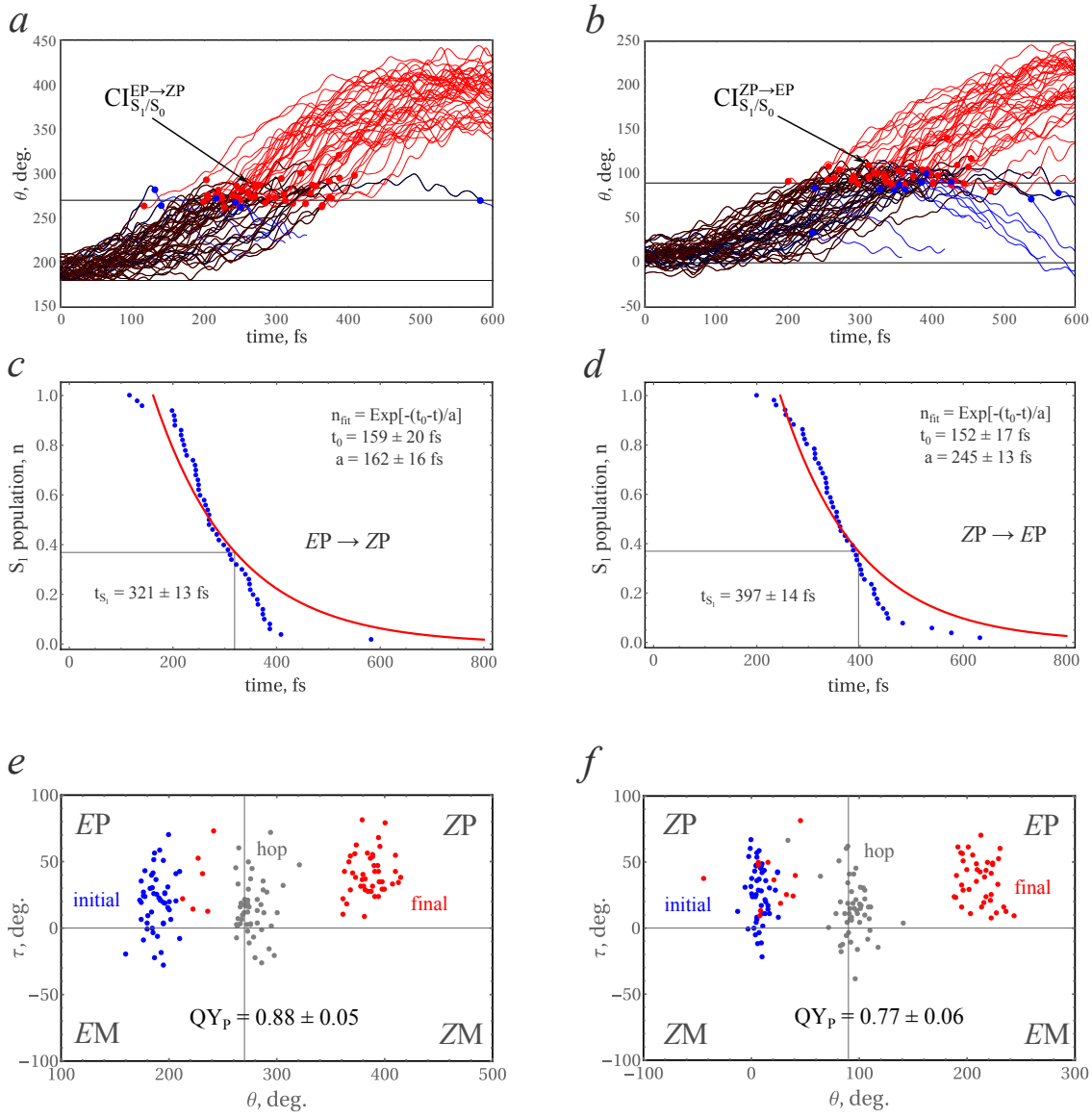

Supplementary Figure 11: Dynamics of the F-MMTDP motor in the gas phase. Panels (a) and (b) show the time evolution of the central dihedral angle θ for the EP $\rightarrow$ ZP and ZP $\rightarrow$ EP photoreactions, respectively. Panels (c) and (d) show the population dynamics of the S_1 state for the two photoreactions. The red curves are fitted to the computed populations (the blue dots) by a monoexponential function $n_{fit}(t) = e^{-(t_0-t)/\tau}$, where t_0 is the latency time and τ is the exponential decay constant. The excited-state lifetimes t_{S_1} are shown in the insets. The margins of error of the fitted quantities were obtained by bootstrapping with 10^4 replicas.[59] Panels (e) and (f) show the distribution of the dihedral angles θ and τ for the EP $\rightarrow$ ZP and ZP $\rightarrow$ EP photoreactions, respectively. The initial structures are shown by the blue dots, the final structures by the red dots, and the structures at the moment of the $S_1 \rightarrow S_0$ transition (hops) by the grey dots. The quantum yields of photoisomerisation for both photoreactions are shown in the insets.

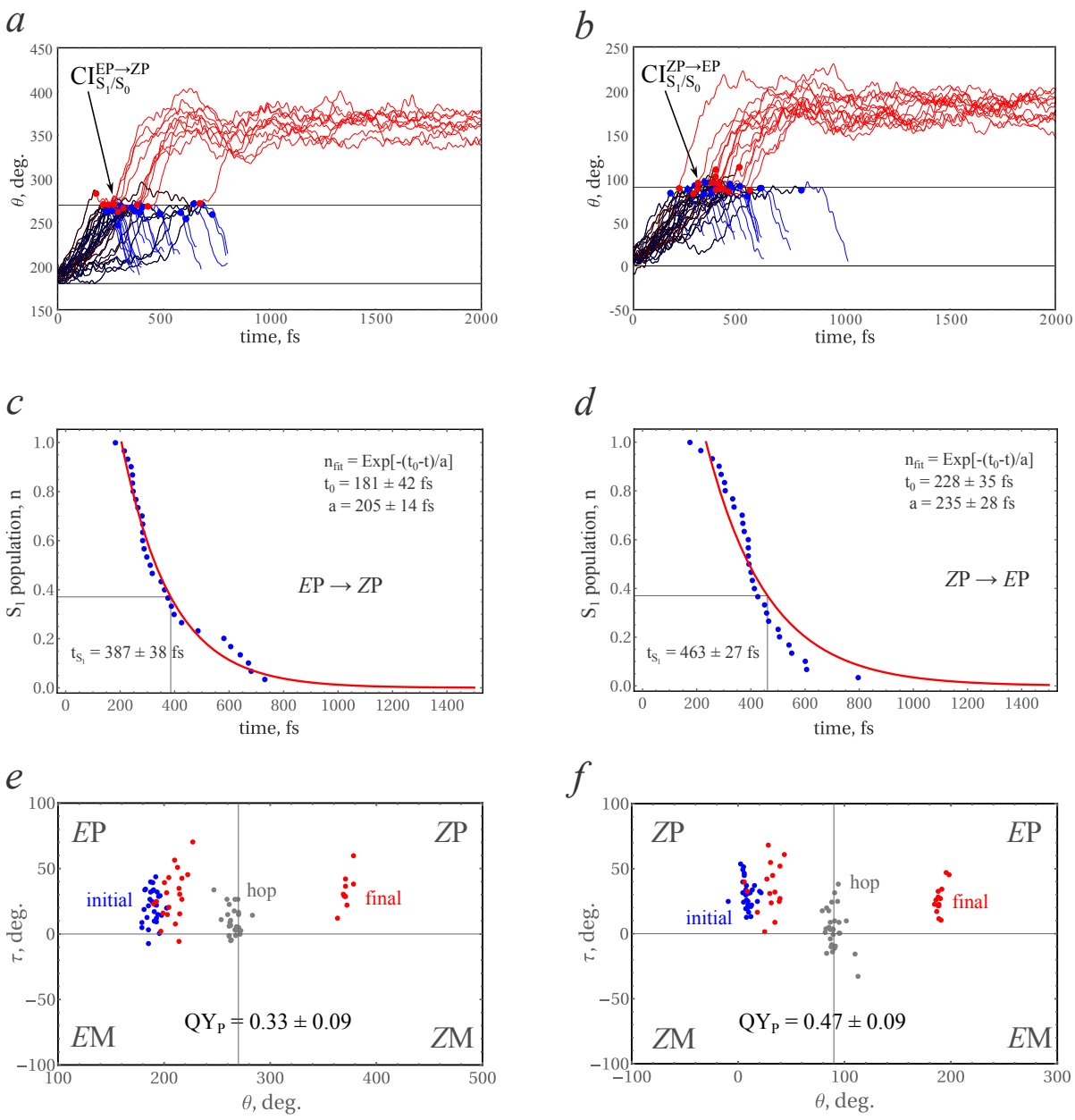

Supplementary Figure 12: Dynamics of the F-MMTDP motor in MeOH. Panels (a) and (b) show the time evolution of the central dihedral angle θ for the EP $\rightarrow$ ZP and ZP $\rightarrow$ EP photoreactions, respectively. Panels (c) and (d) show the population dynamics of the S_1 state for the two photoreactions. The red curves are fitted to the computed populations (the blue dots) by a monoexponential function $n_{fit}(t) = e^{-(t_0-t)/\tau}$, where t_0 is the latency time and τ is the exponential decay constant. The excited-state lifetimes t_{S_1} are shown in the insets. The margins of error of the fitted quantities were obtained by bootstrapping with 10^4 replicas.[59] Panels (e) and (f) show the distribution of the dihedral angles θ and τ for the EP $\rightarrow$ ZP and ZP $\rightarrow$ EP photoreactions, respectively. The initial structures are shown by the blue dots, the final structures by the red dots, and the structures at the moment of the $S_1 \rightarrow S_0$ transition (hops) by the grey dots. The quantum yields of photoisomerisation for both photoreactions are shown in the insets.

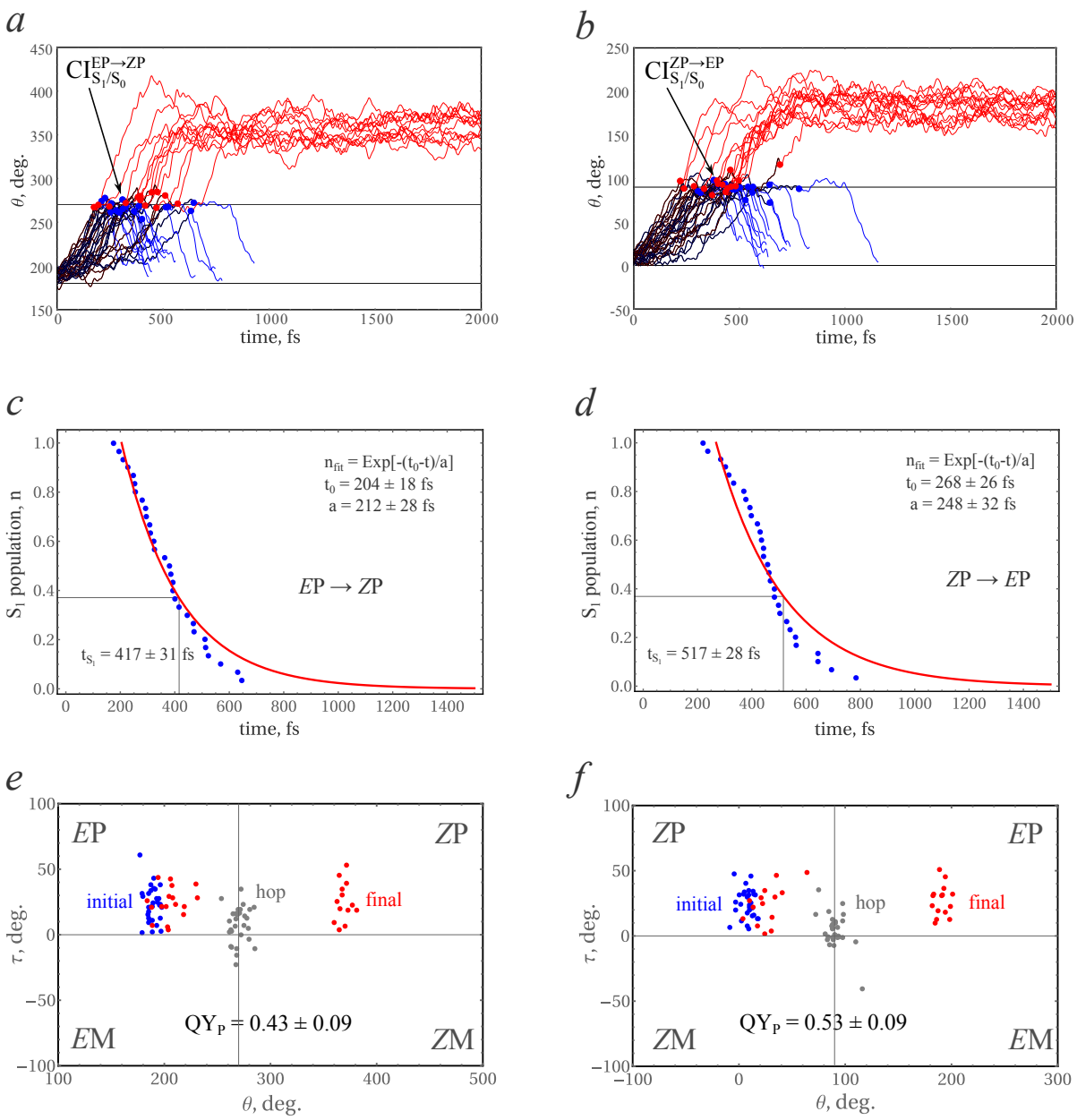

Supplementary Figure 13: Dynamics of the F-MMTDP motor in MeCN. Panels (a) and (b) show the time evolution of the central dihedral angle θ for the EP $\rightarrow$ ZP and ZP $\rightarrow$ EP photoreactions, respectively. Panels (c) and (d) show the population dynamics of the S_1 state for the two photoreactions. The red curves are fitted to the computed populations (the blue dots) by a monoexponential function $n_{fit}(t) = e^{-(t_0-t)/\tau}$, where t_0 is the latency time and τ is the exponential decay constant. The excited-state lifetimes t_{S_1} are shown in the insets. The margins of error of the fitted quantities were obtained by bootstrapping with 10^4 replicas.[59] Panels (e) and (f) show the distribution of the dihedral angles θ and τ for the EP $\rightarrow$ ZP and ZP $\rightarrow$ EP photoreactions, respectively. The initial structures are shown by the blue dots, the final structures by the red dots, and the structures at the moment of the $S_1 \rightarrow S_0$ transition (hops) by the grey dots. The quantum yields of photoisomerisation for both photoreactions are shown in the insets.

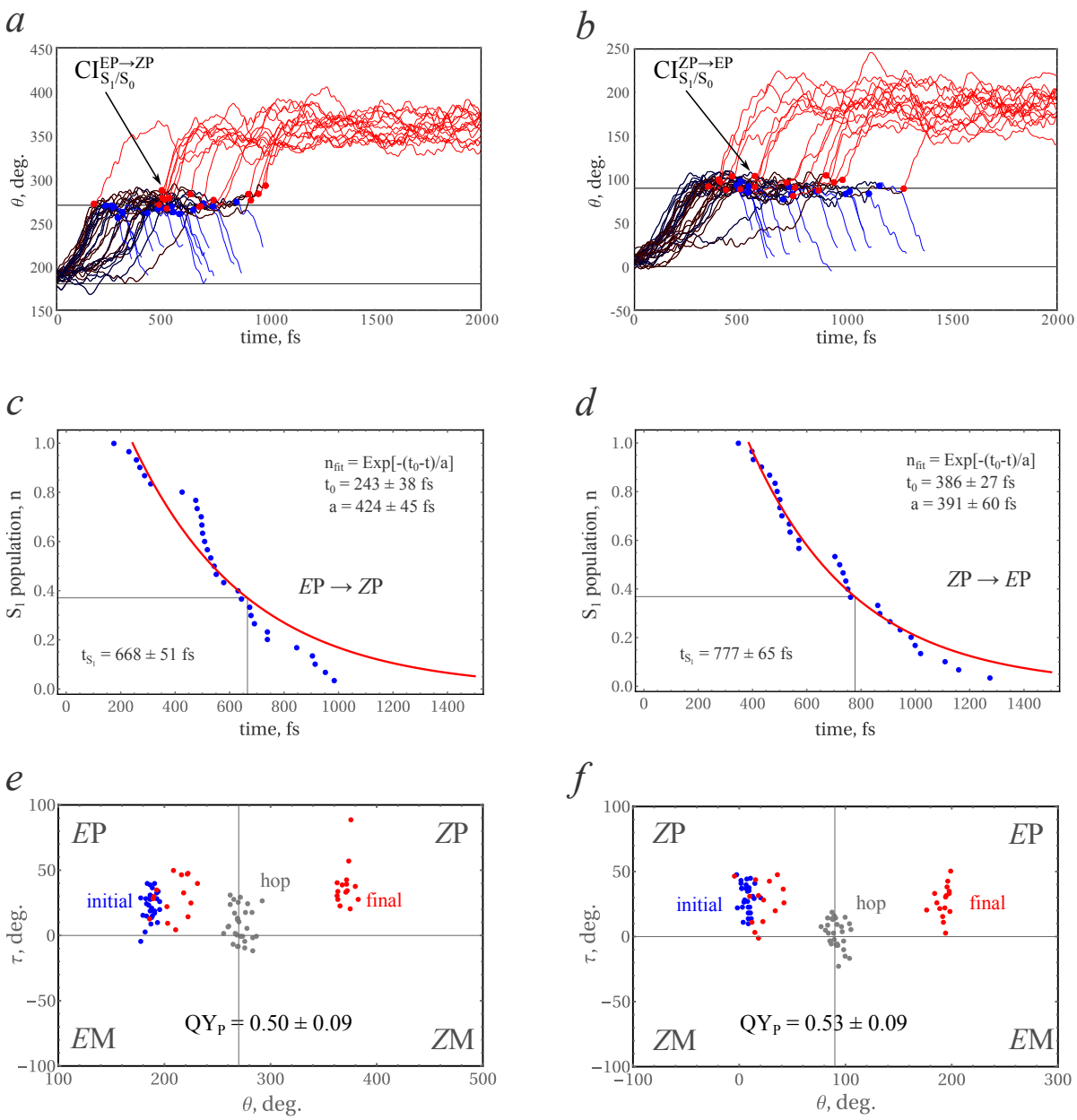

Supplementary Figure 14: Dynamics of the F-MMTDP motor in DCM. Panels (a) and (b) show the time evolution of the central dihedral angle θ for the EP $\rightarrow$ ZP and ZP $\rightarrow$ EP photoreactions, respectively. Panels (c) and (d) show the population dynamics of the S_1 state for the two photoreactions. The red curves are fitted to the computed populations (the blue dots) by a monoexponential function $n_{fit}(t) = e^{-(t_0-t)/\tau}$, where t_0 is the latency time and τ is the exponential decay constant. The excited-state lifetimes t_{S_1} are shown in the insets. The margins of error of the fitted quantities were obtained by bootstrapping with 10^4 replicas.[59] Panels (e) and (f) show the distribution of the dihedral angles θ and τ for the EP $\rightarrow$ ZP and ZP $\rightarrow$ EP photoreactions, respectively. The initial structures are shown by the blue dots, the final structures by the red dots, and the structures at the moment of the $S_1 \rightarrow S_0$ transition (hops) by the grey dots. The quantum yields of photoisomerisation for both photoreactions are shown in the insets.

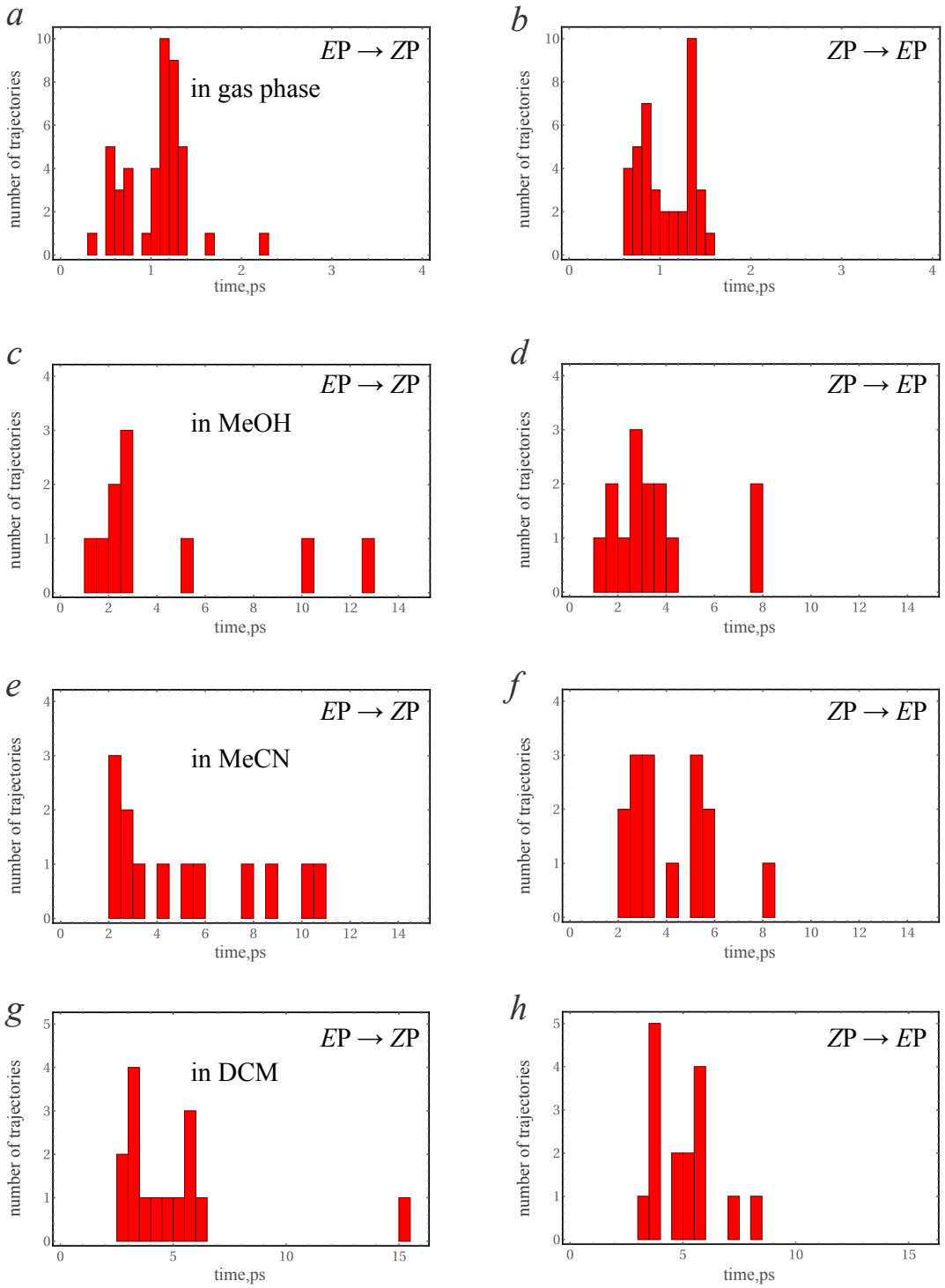

Supplementary Figure 15: Distributions of the time-of-arrival (TOA) at the final structure for the trajectories simulated in the (a) gas phase, (b) MeOH solution, (c) MeCN solution, and (d) DCM solution.

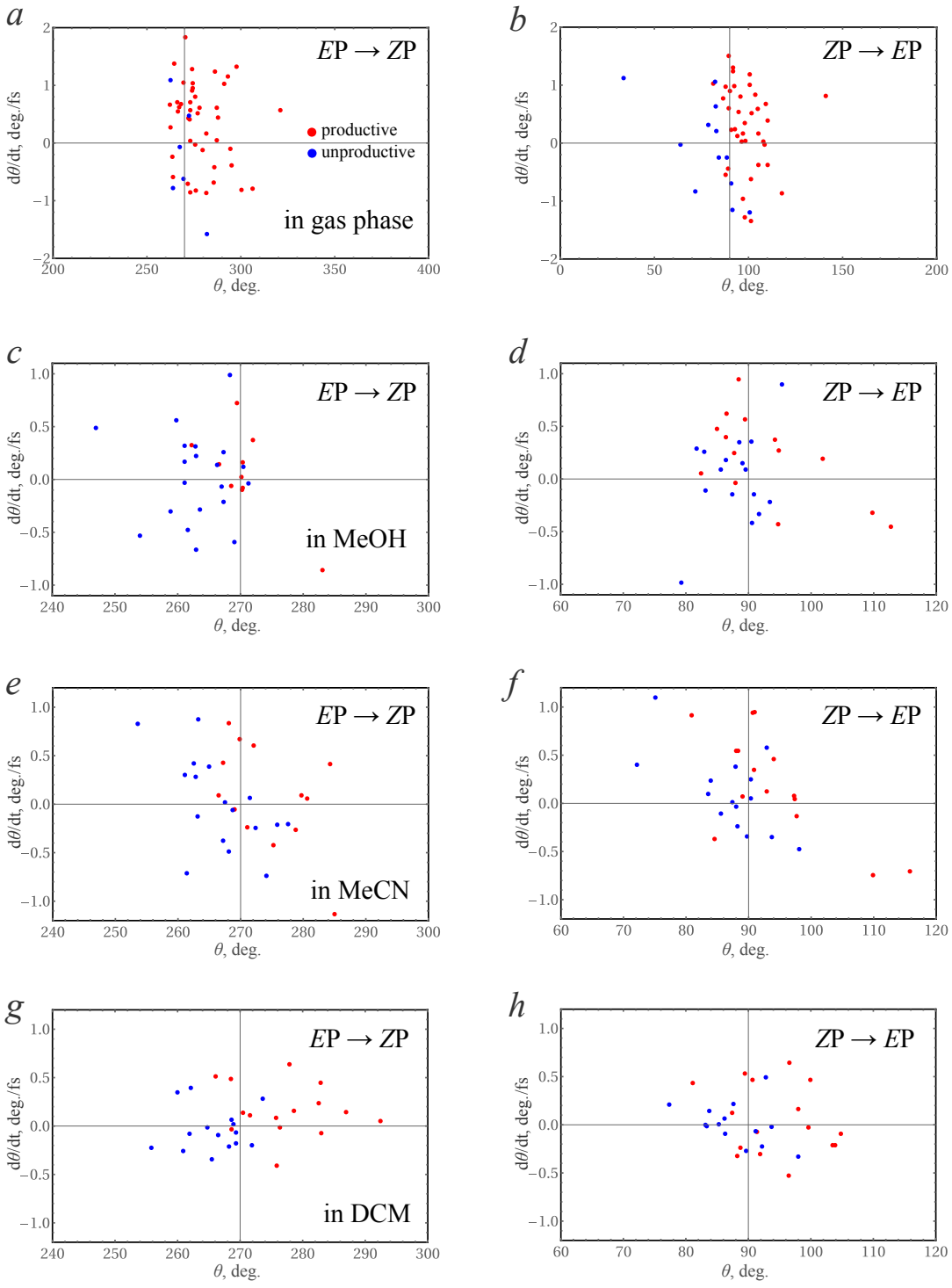

Supplementary Figure 16: Distributions of the central dihedral angle θ and angular velocity $d\theta/dt$ at the time of the $S_1 \rightarrow S_0$ transition (surface hop) for the EP $\rightarrow$ ZP and ZP $\rightarrow$ EP photoreactions. Panels (a) and (b) show the gas phase reactions, (c) and (d) show reactions in MeOH, (e) and (f) in MeCN, and (g) and (h) in DCM. The red dots show the productive trajectories and the blue dots show the unproductive trajectories.

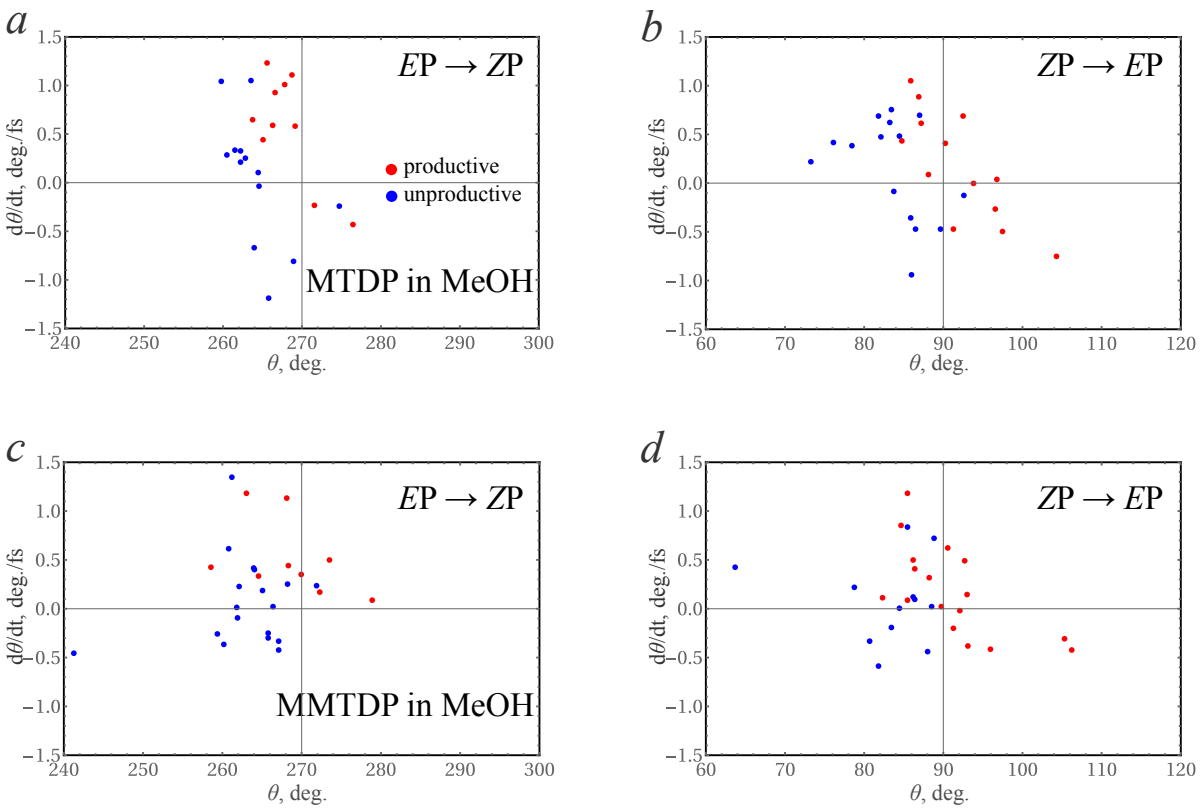

Supplementary Figure 17: Distributions of the central dihedral angle θ and angular velocity $d\theta/dt$ at the time of the $S_1 \rightarrow S_0$ transition (surface hop) for the (a) *E*P → *Z*P and (b) *Z*P → *E*P photoreactions occurring in MTDP (**1**) in MeOH, and (c) *E*P → *Z*P and (d) *Z*P → *E*P photoreactions occurring in MMTDP (**2**) in MeOH. The red dots show the productive trajectories, and the blue dots show the unproductive trajectories. The graphs were plotted using the data from ref.[48].

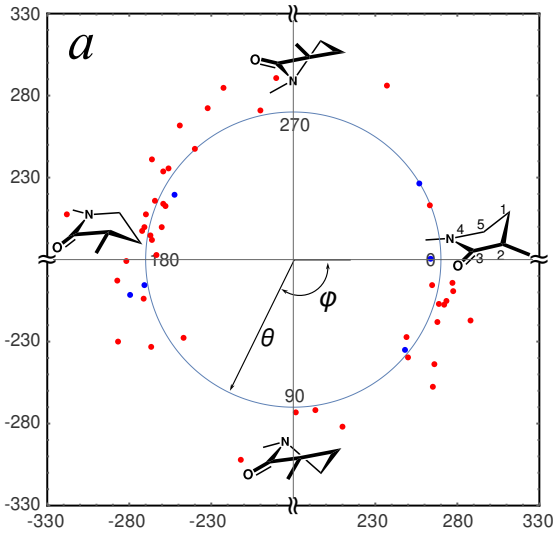
a
330
280
230
-230
-280
-330
-330
-280
-230
230
280
330
270
180
0
90
φ
θ

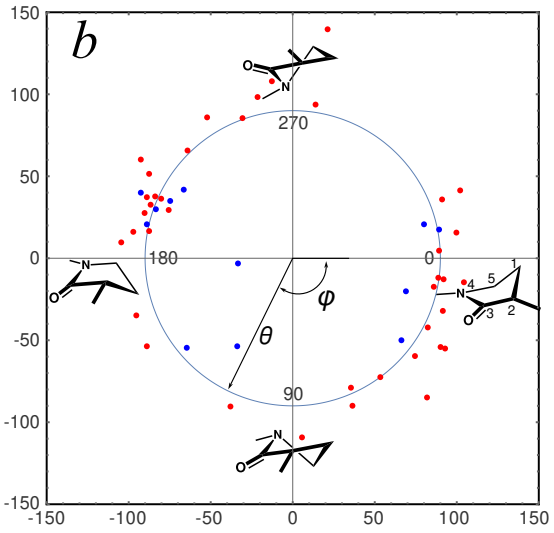
b
150
100
50
0
-50
-100
-150
-150
-100
-50
0
50
100
150
270
180
0
90
φ
θ

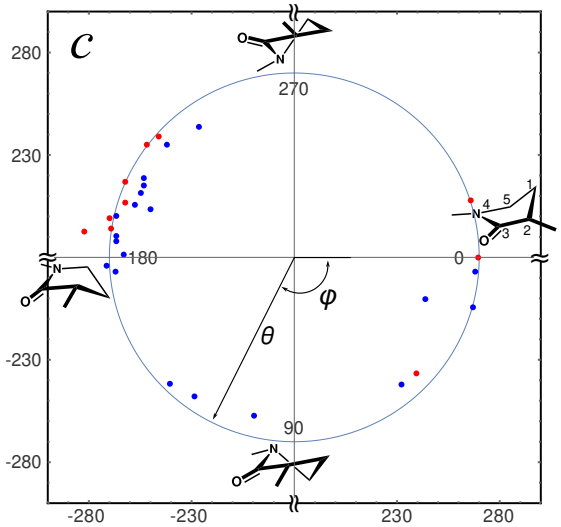
c
280
230
-230
-280
-280
-230
230
280
270
180
0
90
φ
θ

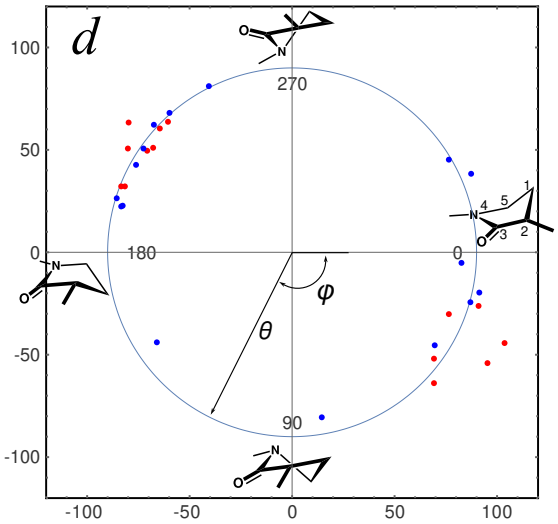
d
100
50
0
-50
-100
-100
-50
0
50
100
270
180
0
90
φ
θ

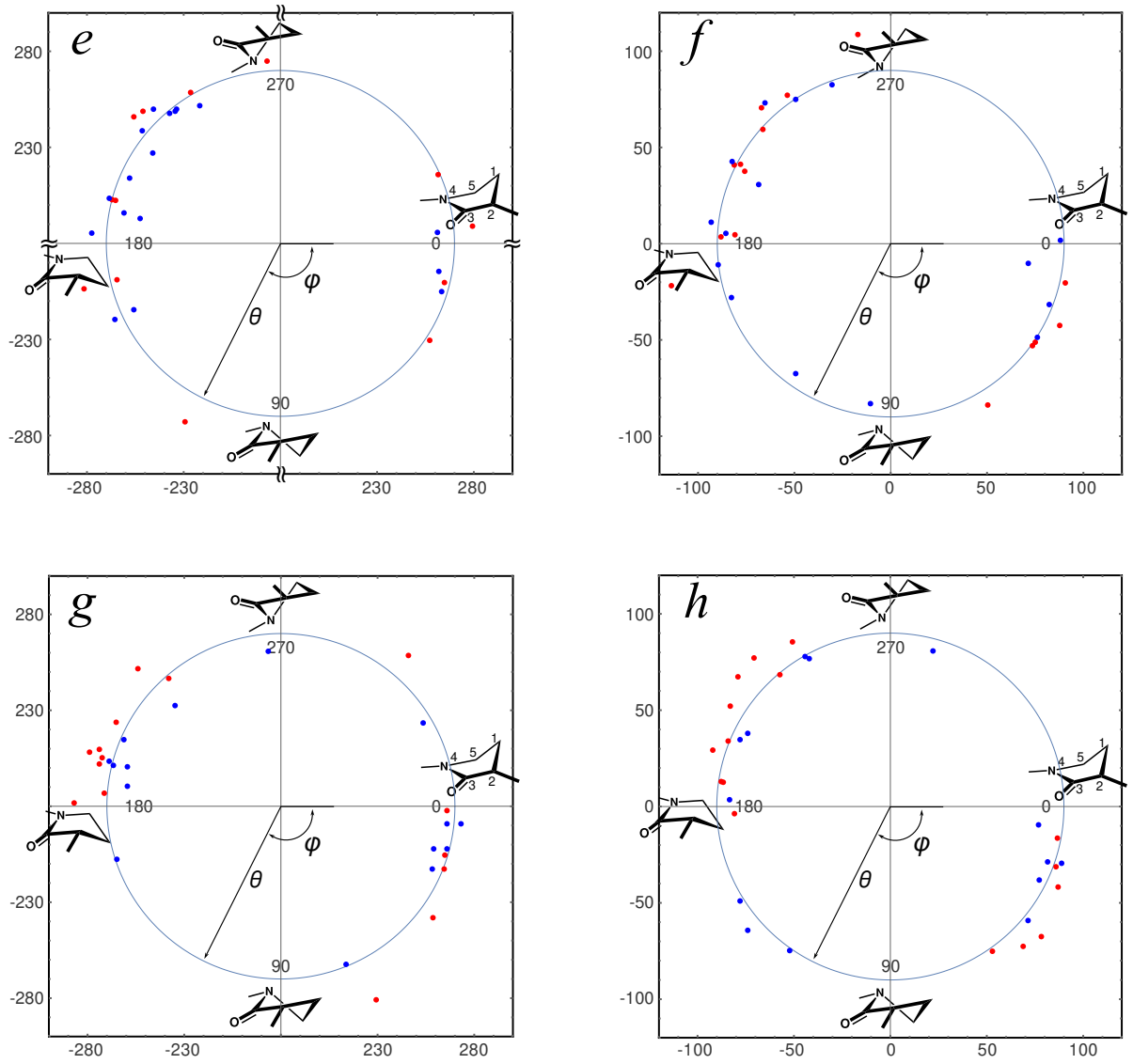

Supplementary Figure 19: Conformations of the pyrrolidinone ring in the motor **3** at the time of the $S_1 \rightarrow S_0$ surface hop. The conformations are characterized by two parameters: the central dihedral angle θ and the Cremer-Pople puckering angle[50] ϕ. The numbering of the atoms in the ring, used when calculating the puckering angle, is given in the insets. The circles of fixed radius show the threshold values of the angle θ used in Figure 16; θ = 270° for EP $\rightarrow$ ZP and θ = 90° for ZP $\rightarrow$ EP. The red dots show the (θ, ϕ) values for the productive trajectories and the blue dots for the unproductive trajectories. Panels (a) and (b) show the distribution of the (θ, ϕ) values for the EP $\rightarrow$ ZP and ZP $\rightarrow$ EP reactions in the gas phase, respectively. Panels (c) and (d) show the same distributions for photoreactions in MeOH. Panels (e) and (f) show photoreactions in MeCN, and panels (g) and (h) in DCM.

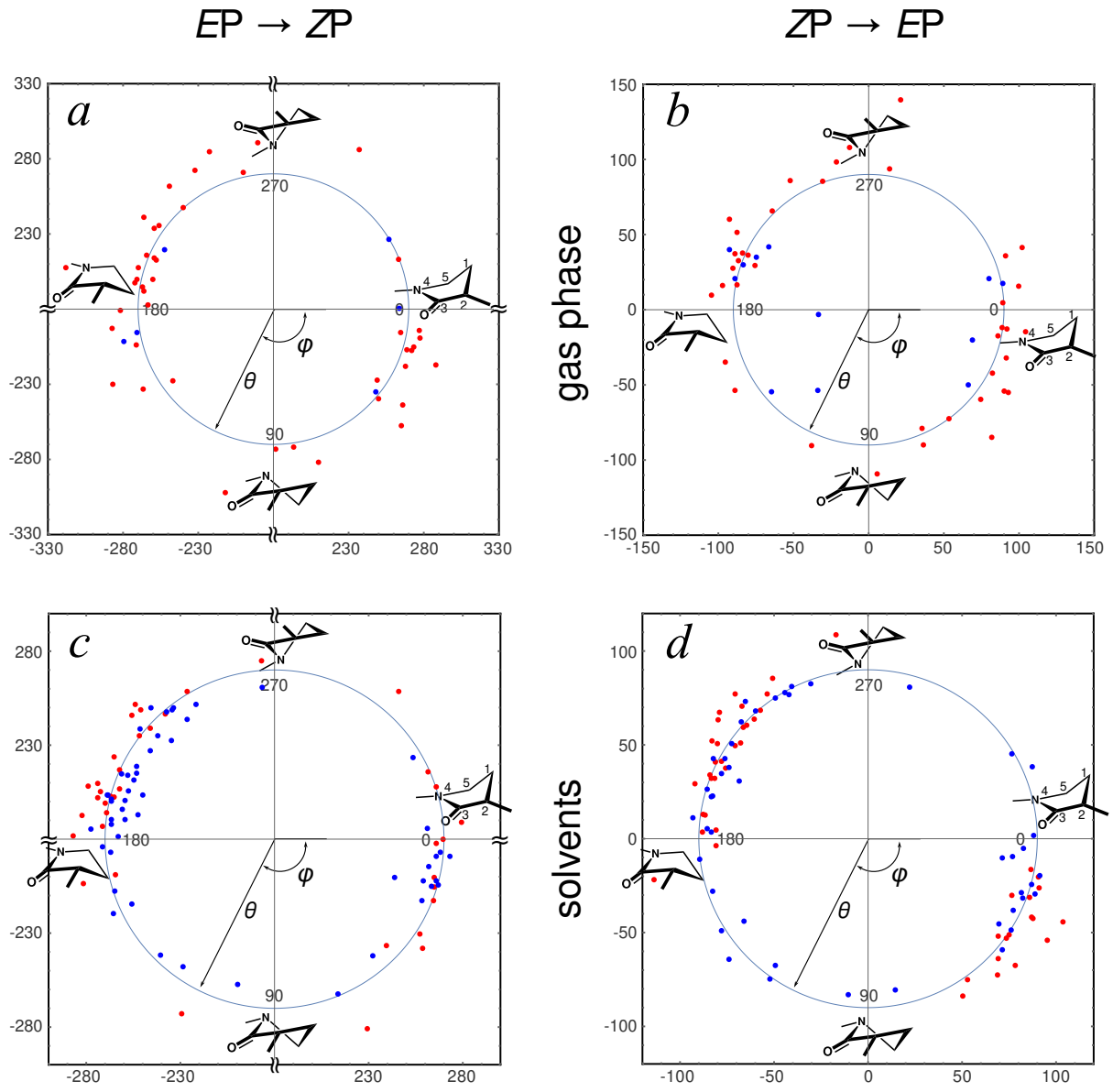

Supplementary Figure 20: Conformations of the pyrrolidinone ring in the motor **3** at the time of the $S_1 \rightarrow S_0$ surface hop. The conformations are characterized by two parameters: the central dihedral angle θ and the Cremer-Pople puckering angle[50] ϕ. The numbering of the atoms in the ring, used when calculating the puckering angle, is given in the insets. The circles of fixed radius show the threshold values of the angle θ used in Figure 16; θ = 270° for EP → ZP and θ = 90° for ZP → EP. The red dots show the (θ, ϕ) values for the productive trajectories and the blue dots for the unproductive trajectories. Panels (a) and (b) show the distribution of the (θ, ϕ) values for the EP → ZP and ZP → EP reactions in the gas phase, respectively. Panels (c) and (d) show the same distributions for photoreactions in all solvents considered in the QM/MM simulations; i.e., MeOH, MeCN, and DCM.

Supplementary Table 2 shows the analysis of the $S_1 \rightarrow S_0$ hopping times, where the average times for F-MMTDP in various media are shown together with the standard deviation (std) as mean $\pm$ std. The hopping times $t_{2\mathrm{hop}}$ are divided into two contributions: one is the time $t_{2\mathrm{NACR}}$ required to reach the region of strong nonadiabatic coupling (NACR) and the other is the time $t_{in\mathrm{NACR}}$ spent within the region of strong nonadiabatic coupling. As seen in Supplementary Fig. 16, nearly all surface hops occur in the region within $\pm 20^\circ$ of the dividing line between the reactants and products. Therefore, the region of strong nonadiabatic coupling was defined by the angle θ within the range of values starting from 250° for *E*P $\rightarrow$ *Z*P and 90° for *Z*P $\rightarrow$ *E*P.

In the gas phase, the largest contribution to $t_{2\mathrm{hop}}$ is the time required to reach the region of strong coupling. The time spent within this region is approximately 40–45% of this value. The situation remains mainly the same in the MeON and MeCN solvents, where the longest contribution to $t_{2\mathrm{hop}}$ is from $t_{2\mathrm{NACR}}$. In DCM, this changes and it is $t_{in\mathrm{NACR}}$ that makes the greatest contribution to $t_{2\mathrm{hop}}$, while $t_{2\mathrm{NACR}}$ remains basically the same as in other solvents and gas phase.

MTDP in the gas phase takes a somewhat longer time to reach the region of strong coupling during the *E*P $\rightarrow$ *Z*P reaction. This is explained by the effect of the O$\cdots$F repulsion in F-MMTDP, which accelerates the torsion in the early stage of the photoreaction. Very little difference is observed for the *Z*P $\rightarrow$ *E*P step. In MeOH, MTDP and F-MMTDP show very similar characteristics of the hopping times. The greatest difference between F-MMTDP and its parent molecules is with MMTDP, where, during the *E*P $\rightarrow$ *Z*P reaction, torsion towards the strong coupling region twice the time. This is likely caused by the effect of the intramolecular attractive interactions, which retard the movement towards the conical intersection seam.

For some selected QM/MM NAMD trajectories, the geometries of the minimum-energy conical intersections (MECI) and S_1 minima have been optimised starting from the snapshots at the hopping time. The resulting energies are reported in Supplementary

Supplementary Table 2: Analysis of times to $S_1 \rightarrow S_0$ surface hop in F-MMTDP, MMTDP, and MTDP in various media. The following characteristics are reported: $t_{2\text{hop}}$ - a time spent in the S_1 state until the surface hop; $t_{2\text{NACR}}$ - a time required to reach the region of strong nonadiabatic coupling (when the torsion angle θ reaches 70° from the starting structure; that is, $\theta = 250°$ for *EP* $\rightarrow$ *ZP* and $\theta = 70°$ for *ZP* $\rightarrow$ *EP*); $t_{in\text{NACR}}$ - a time spent within the region of strong nonadiabatic coupling before hop. The numeric values are given as mean $\pm$ std**, where std is the standard deviation.**

medium	reaction	$t_{2\text{hop}}$, fs	$t_{2\text{NACR}}$, fs	$t_{in\text{NACR}}$, fs
		F-MMTDP		
gas phase	*EP* $\rightarrow$ *ZP*	283 ± 82	205 ± 63	78 ± 50
	ZP $\rightarrow$ *EP*	365 ± 84	250 ± 70	115 ± 74
MeOH	*EP* $\rightarrow$ *ZP*	372 ± 158	261 ± 115	111 ± 120
	ZP $\rightarrow$ *EP*	410 ± 127	269 ± 88	141 ± 92
MeCN	*EP* $\rightarrow$ *ZP*	374 ± 127	275 ± 118	99 ± 70
	ZP $\rightarrow$ *EP*	457 ± 130	291 ± 92	166 ± 88
DCM	*EP* $\rightarrow$ *ZP*	568 ± 219	264 ± 118	304 ± 208
	ZP $\rightarrow$ *EP*	709 ± 254	295 ± 132	414 ± 267
		MMTDP		
MeOH	*EP* $\rightarrow$ *ZP*	652 ± 419	588 ± 385	64 ± 61
	ZP $\rightarrow$ *EP*	361 ± 195	272 ± 172	89 ± 55
		MTDP		
gas phase	*EP* $\rightarrow$ *ZP*	370 ± 64	324 ± 52	46 ± 50
	ZP $\rightarrow$ *EP*	281 ± 45	223 ± 30	58 ± 38
MeOH	*EP* $\rightarrow$ *ZP*	390 ± 189	292 ± 210	98 ± 111
	ZP $\rightarrow$ *EP*	302 ± 113	226 ± 96	76 ± 50

Table 3, where they are compared with the gas phase geometry optimisations.

As seen in the table, the MECI geometries in the gas phase and MeOH and MeCN

Supplementary Table 3: Energies of the MECI structures and S_1 minima obtained for F-MMTDP in the gas phase and various solvents. For the latter, the geometries of MECI and S_1 minima were optimized for randomly selected trajectories. The energies are given in the atomic units in the following order: S_0 energy / S_1 energy.

medium	geometry	*E*P → *Z*P	*Z*P → *E*P
		F-MMTDP	
gas phase	MECI	-1284.815241 / -1284.815123	-1284.807118 / -1284.806990
	$S_{1,min}$	-1284.829370 / -1284.816355	-1284.827968 / -1284.809623
MeOH	MECI	-1285.511046 / -1285.510933	-1285.497033 / -1285.496982
	$S_{1,min}$	-1285.519370 / -1285.511736	—[a)]
MeCN	MECI	-1286.452198 / -1286.452083	-1286.588414 / -1286.588307
	$S_{1,min}$	-1286.471122 / -1286.454118	-1286.594934 / -1286.588864
DCM	MECI	-1255.164351 / -1255.164207	-1236.370859 / -1236.370771
	$S_{1,min}$	-1255.183322 / -1255.168121	-1236.384683 / -1236.375000
		MMTDP	
MeOH	MECI	-1186.381437 / -1186.381367	-1186.359001 / -1186.358955
	$S_{1,min}$	—[a)]	—[a)]
		MTDP	
gas phase	MECI	-1146.332571 / -1146.332557	-1146.332365 / -1146.332350
	$S_{1,min}$	—[a)]	—[a)]
MeOH	MECI	-1147.032463 / -1147.032392	-1147.051732 / -1147.051668
	$S_{1,min}$	—[a)]	—[a)]

[a)] Oscillatory convergence; MECI occurs at the bottom of the S_1 minimum.

solvents correspond to peaked topography. In the gas phase, the MECI energies are elevated above the respective S_1 minima by 0.8 – 1.7 kcal/mol. In MeOH, the elevation is

$\lesssim$ 0.5 kcal/mol. In the *Z*P $\rightarrow$ *E*P step, MECI occurs at the bottom of the S_1 minimum. In MeCN, the MECI elevation is 0.3 – 1.3 kcal/mol. These values correspond to peaked or nearly so topographies of the respective MECIs. In DCM, the MECI geometries are elevated by more than 3 kcal/mol. This suggests that these MECIs have a sloped topography. In both MTDP and MMTDP, MECIs have peaked topography, both in the gas phase and in MeOH.

Supplementary References

(1) Landaluce, T. F.; London, G.; Pollard, M. M.; Rudolf, P.; Feringa, B. L. Rotary Molecular Motors: A Large Increase in Speed through a Small Change in Design. *J. Org. Chem.* **2010**, *75*, 5323–5325.

(2) Štacko, P.; Kistemaker, J. C. M.; Feringa, B. L. Fluorine-Substituted Molecular Motors with a Quaternary Stereogenic Center. *Chem. Eur. J.* **2017**, *23*, 6643–6653.

(3) Paolino, M.; Gueye, M.; Pieri, E.; Manathunga, M.; Fusi, S.; Cappelli, A.; Latterini, L.; Pannacci, D.; Filatov, M.; Léonard, J. et al. Design, Synthesis, and Dynamics of a Green Fluorescent Protein Fluorophore Mimic with an Ultrafast Switching Function. *J. Am. Chem. Soc.* **2016**, *138*, 9807–9825.

(4) Filatov(Gulak), M.; Paolino, M.; Pierron, R.; Cappelli, A.; Giorgi, G.; Léonard, J.; Huix-Rotllant, M.; Ferré, N.; Yang, X.; Kaliakin, D. et al. Towards the engineering of a photon-only two-stroke rotary molecular motor. *Nat. Comm.* **2022**, *13*, 6433.

(5) Filatov, M.; Shaik, S. A spin-restricted ensemble-referenced Kohn-Sham method and its application to diradicaloid situations. *Chem. Phys. Lett.* **1999**, *304*, 429–437.

(6) Moreira, I. d. P. R.; Costa, R.; Filatov, M.; Illas, F. Restricted ensemble-referenced Kohn-Sham versus broken symmetry approaches in density functional theory: Magnetic coupling in Cu binuclear complexes. *J. Chem. Theory Comput.* **2007**, *3*, 764–774.

(7) Kazaryan, A.; Heuver, J.; Filatov, M. Excitation Energies from Spin-Restricted Ensemble-Referenced Kohn-Sham Method: A State-Average Approach†. *J. Phys. Chem. A* **2008**, *112*, 12980–12988.

(8) Filatov, M. Assessment of density functional methods for obtaining geometries at conical intersections in organic molecules. *J. Chem. Theory Comput.* **2013**, *9*, 4526–4541.

(9) Filatov, M. Spin-restricted ensemble-referenced Kohn-Sham method: basic principles and application to strongly correlated ground and excited states of molecules. *WIREs Comput. Mol. Sci.* **2015**, *5*, 146–167.

(10) Filatov, M. In *Density-functional methods for excited states*; Ferré, N., Filatov, M., Huix-Rotllant, M., Eds.; Top. Curr. Chem.; Springer: Heidelberg, 2016; Vol. 368; pp 97–124.

(11) Valone, S. M. A one-to-one mapping between one-particle densities and some n-particle ensembles. *J. Chem. Phys.* **1980**, *73*, 4653–4655.

(12) Lieb, E. H. Density functionals for Coulomb systems. *Int. J. Quantum Chem.* **1983**, *24*, 243–277.

(13) Perdew, J. P.; Parr, R. G.; Levy, M.; Balduz Jr., J. L. Density-Functional Theory for Fractional Particle Number: Derivative Discontinuities of the Energy. *Phys. Rev. Lett.* **1982**, *49*, 1691–1694.

(14) Englisch, H.; Englisch, R. Hohenberg-Kohn Theorem and Non-V-Representable Densities. *Physica* **1983**, *A121*, 253–268.

(15) Englisch, H.; Englisch, R. Exact Density Functionals for Ground-State Energies. I. General Results. *Phys. Stat. Sol. (b)* **1984**, *123*, 711–721.

(16) Englisch, H.; Englisch, R. Exact Density Functionals for Ground-State Energies II. Details and Remarks. *Phys. Stat. Sol. (b)* **1984**, *124*, 373–379.

(17) Gross, E. K. U.; Oliveira, L. N.; Kohn, W. Rayleigh-Ritz variational principle for ensembles of fractionally occupied states. *Phys. Rev. A* **1988**, *37*, 2805–2808.

(18) Gross, E. K. U.; Oliveira, L. N.; Kohn, W. Density-functional theory for ensembles of fractionally occupied states. I. Basic formalism. *Phys. Rev. A* **1988**, *37*, 2809–2820.

(19) Oliveira, L. N.; Gross, E. K. U.; Kohn, W. Density-functional theory for ensembles of fractionally occupied states. II. Application to the He atom. *Phys. Rev. A* **1988**, *37*, 2821–2833.

(20) Oliveira, L. N.; Gross, E. K. U.; Kohn, W. Ensemble-Density Functional Theory. *Int. J. Quantum Chem.: Quantum Chem. Symp.* **1990**, *24*, 707–716.

(21) Filatov, M.; Liu, F.; Martínez, T. J. Analytical derivatives of the individual state energies in ensemble density functional theory method. I. General formalism. *J. Chem. Phys.* **2017**, *147*, 034113.

(22) Filatov, M.; Lee, S.; Choi, C. H. Computation of Molecular Ionization Energies Using an Ensemble Density Functional Theory Method. *J. Chem. Theory Comput.* **2020**, *16*, 4489–4504.

(23) Filatov, M.; Lee, S.; Choi, C. H. Description of Sudden Polarization in the Excited Electronic States with an Ensemble Density Functional Theory Method. *J. Chem. Theory Comput.* **2021**, *17*, 5123–5139.

(24) Ha, J.-K.; Lee, I. S.; Min, S. K. Surface Hopping Dynamics beyond Nonadiabatic Couplings for Quantum Coherence. *J. Phys. Chem. Lett.* **2018**, *9*, 1097–1104.

(25) Lee, I. S.; Ha, J.-K.; Han, D.; Kim, T. I.; Moon, S. W.; Min, S. K. PyUNIxMD: A Python-based excited state molecular dynamics package. *J. Comp. Chem.* **2021**, *42*, 1755–1766.

(26) Hunter, G. Conditional probability amplitudes in wave mechanics. *Int. J. Quantum Chem.* **1975**, *9*, 237–242.

(27) Abedi, A.; Maitra, N. T.; Gross, E. K. U. Exact factorization of the time-dependent electron-nuclear wave function. *Phys. Rev. Lett.* **2010**, *105*, 123002.

(28) Abedi, A.; Maitra, N. T.; Gross, E. K. U. Correlated electron-nuclear dynamics: Exact factorization of the molecular wave-function. *J. Chem. Phys.* **2012**, *137*, 22A530.

(29) Abedi, A.; Agostini, F.; Suzuki, Y.; Gross, E. K. U. Dynamical steps that bridge piecewise adiabatic shapes in the exact time-dependent potential energy surface. *Phys. Rev. Lett.* **2013**, *110*, 263001.

(30) Agostini, F.; Abedi, A.; Suzuki, Y.; Min, S. K.; Maitra, N. T.; Gross, E. K. U. The exact electronic back-reaction on classical nuclei in non-adiabatic charge transfer. *J. Chem. Phys.* **2015**, *142*, 084303.

(31) Tully, J. C. Molecular dynamics with electronic transitions. *J. Chem. Phys.* **1990**, *93*, 1061.

(32) Granucci, G.; Persico, M.; Zoccante, A. Including quantum decoherence in surface hopping. *J. Chem. Phys.* **2010**, *133*, 134111.

(33) Hammes-Schiffer, S.; Tully, J. C. Proton transfer in solution: Molecular dynamics with quantum transitions. *J. Chem. Phys.* **1994**, *101*, 4657–4667.

(34) Schmidt, M. W.; Baldridge, K. K.; Boatz, J. A.; Elbert, S. T.; Gordon, M. S.; Jensen, J. J.; Koseki, S.; Matsunaga, N.; Nguyen, K. A.; Su, S. et al. *J. Comput. Chem.* **1993**, *14*, 1347–1363.

(35) Gordon, M.; Schmidt, M. In *Theory and Applications of Computational Chemistry, the first forty years*; Dykstra, C. E., Frenking, G., Kim, K. S., Scuseria, G. E., Eds.; Elsevier: Amsterdam, 2005; pp 1167–1189.

(36) Krishnan, R.; Binkley, J. S.; Seeger, R.; Pople, J. A. Self-consistent molecular orbital methods. XX. A basis set for correlated wave functions. *J. Chem. Phys.* **1980**, *72*, 650–654.

(37) Becke, A. D. Density-Functional Exchange-Energy Approximation with Correct Asymptotic Behavior. *Phys. Rev. A* **1988**, *38*, 3098–3100.

(38) Lee, C.; Yang, W.; Parr, R. G. Development of the Colle-Salvetti Correlation-Energy Formula into a Functional of the Electron Density. *Phys. Rev. B* **1988**, *37*, 785–789.

(39) Becke, A. D. A New Mixing of Hartree-Fock and Local Density-Functional Theories. *J. Chem. Phys.* **1993**, *98*, 1372–1377.

(40) Kästner, J.; Carr, J. M.; Keal, T. W.; Thiel, W.; Wander, A.; Sherwood, P. DL-FIND: An Open-Source Geometry Optimizer for Atomistic Simulations. *J. Phys. Chem. A* **2009**, *113*, 11856–11865.

(41) Kim, T. I.; Ha, J.-K.; Min, S. K. Coupled- and Independent-Trajectory Approaches Based on the Exact Factorization Using the PyUNIxMD Package. *Top. Curr. Chem.* **2022**, *380*, 8.

(42) Baeck, K. K.; An, H. Practical approximation of the non-adiabatic coupling terms for same-symmetry interstate crossings by using adiabatic potential energies only. *J. Chem. Phys.* **2017**, *146*, 064107.

(43) An, H.; Baeck, K. K. Practical and reliable approximation of nonadiabatic coupling terms between triplet electronic states using only adiabatic potential energies. *Chem. Phys. Lett.* **2018**, *696*, 100–105.

(44) T. do Casal, M.; Toldo, J. M.; Pinheiro Jr, M.; Barbatti, M. Fewest switches surface hopping with Baeck-An couplings [version 2; peer review: 3 approved]. *Open Research Europe* **2022**, *1*.

(45) Shu, Y.; Zhang, L.; Chen, X.; Sun, S.; Huang, Y.; Truhlar, D. G. Nonadiabatic Dynamics Algorithms with Only Potential Energies and Gradients: Curvature-Driven Coherent Switching with Decay of Mixing and Curvature-Driven Trajectory Surface Hopping. *J. Chem. Theory Comput.* **2022**, *18*, 1320–1328.

(46) Ponder, F. M., J. W .; Richards TINKER Molecular Modeling Package. *J. Comput. Chem.* **1987**, *8*, 1016–1024.

(47) Caleman, C.; van Maaren, P. J.; Hong, M.; Hub, J. S.; Costa, L. T.; van der Spoel, D. Force Field Benchmark of Organic Liquids: Density, Enthalpy of Vaporization, Heat Capacities, Surface Tension, Isothermal Compressibility, Volumetric Expansion Coefficient, and Dielectric Constant. *J. Chem. Theory Comput.* **2012**, *8*, 61–74.

(48) Filatov(Gulak), M.; Paolino, M.; Kaliakin, D.; Olivucci, M.; Kraka, E.; Min, S. K. Impact of solvation on the photoisomerisation dynamics of a photon-only rotary molecular motor. *Commun. Phys.* **2024**, *7*, 219.

(49) Blanco-González, A.; Kaliakin, D.; Filatov(Gulak), M.; Paolino, M.; Léonard, J.; Olivucci, M. Population Dynamics of a Photon-only Molecular Motor Shows that Mode Synchronization and Transient Binding Determine the Rotary Quantum Efficiency. *J. Chem. Theory Comput.* **2025**, *under review*.

(50) Cremer, D.; Pople, J. A. General definition of ring puckering coordinates. *J. Am. Chem. Soc.* **1975**, *97*, 1354–1358.

(51) Jónsson, H.; Mills, G.; Jacobsen, K. W. In *Classical and Quantum Dynamics in Condensed Phase Simulations*; Berne, B. J., Ciccotti, G., Coker, D. F., Eds.; World Scientific: Singapore, 1998; Chapter 16, pp 385–404.

(52) Kazaryan, A.; Kistemaker, J. C. M.; Schäfer, L. V.; Browne, W. R.; Feringa, B. L.; Filatov, M. Understanding the Dynamics Behind the Photoisomerization of a Light-Driven Fluorene Molecular Rotary Motor. *J. Phys. Chem. A* **2010**, *114*, 5058–5067.

(53) Kazaryan, A.; Lan, Z.; Schäfer, L. V.; Thiel, W.; Filatov, M. Surface Hopping Excited-State Dynamics Study of the Photoisomerization of a Light-Driven Fluorene Molecular Rotary Motor. *J. Chem. Theory Comput.* **2011**, *7*, 2189–2199.

(54) Filatov, M.; Olivucci, M. Designing conical intersections for light-driven single molecule rotary motors: From precessional to axial motion. *J. Org. Chem.* **2014**, *79*, 3587–3600.

(55) Nikiforov, A.; Gamez, J. A.; Thiel, W.; Filatov, M. Computational Design of a Family of Light-Driven Rotary Molecular Motors with Improved Quantum Efficiency. *J. Phys. Chem. Lett.* **2016**, *7*, 105–110.

(56) Pronk, S.; Páll, S.; Schulz, R.; Larsson, P.; Bjelkmar, P.; Apostolov, R.; Shirts, M. R.; Smith, J. C.; Kasson, P. M.; van der Spoel, D. et al. GROMACS 4.5: a high-throughput and highly parallel open source molecular simulation toolkit. *Bioinformatics* **2013**, *29*, 845–854.

(57) Kawai, S.; Canova, F. F.; Glatzel, T.; Foster, A. S.; Meyer, E. Atomic-scale dissipation processes in dynamic force spectroscopy. *Phys. Rev. B* **2011**, *84*, 115415.

(58) Aldaz, C. R.; Martínez, T. J.; Zimmerman, P. M. The Mechanics of the Bicycle Pedal Photoisomerization in Crystalline cis,cis-1,4-Diphenyl-1,3-butadiene. *J. Phys. Chem. A* **2020**, *124*, 8897–8906.

(59) Nangia, S.; Jasper, A. W.; Miller, T. F.; Truhlar, D. G. Army ants algorithm for rare event sampling of delocalized nonadiabatic transitions by trajectory surface hopping and the estimation of sampling errors by the bootstrap method. *J. Chem. Phys.* **2004**, *120*, 3586–3597.